Statistical tool for the detection of intrinsic signals measured by optical imaging

Pierre Bouillot and Shahan Momjian

Geneva University Hospitals
Department of Clinical Neurosciences, Service of Neurosurgery

June 5, 2012

Abstract

We provide a description of the statistical tool "OIS detection" devoted to the detection of epilepsy and stimulation related neuronal excitations. This tool is based on the technique of optical imaging of intrinsic signals (OIS) which is shortly reminded in this document as well as the technical details of the statistical methods used in the implemented detection processes. We show that the most robust algorithm requires a registration precomputational step for correcting the cortical movement, a wavelet decomposition and a time whitening step in order to deal with the spatial and the time correlations, respectively.

Contents

1 Optical imaging of intrinsic signals (OIS) 2

2 Introduction 2
- 2.1 Beer-Lambert . . . 2
- 2.2 Typical signals . . . 3
- 2.3 Linear response . . . 4
- 2.4 Data acquisition . . . 5
- 2.5 Artificial data . . . 6

3 Detection methods 7
- 3.1 General linear model (GLM) . . . 8
- 3.2 Registration . . . 10
- 3.3 Glare detection . . . 13
- 3.4 Spatial filtering . . . 13
- 3.5 Time corrections . . . 16
  - 3.5.1 Time filtering . . . 16
  - 3.5.2 Time whitening . . . 19
- 3.6 Wavelet . . . 22

4 Software description 27
- 4.1 Acquisition parameters . . . 28
- 4.2 Detection parameters . . . 29

5 Conclusions 30

1 Optical imaging of intrinsic signals (OIS)

Optical imaging of intrinsic signals (OIS) is a promising technique [14, 15] for measuring the cortical light reflectance changes related to the neuronal activity. The light reflectance is measured with a charge-coupled device (CCD) camera after being filtered through a bandpass filter (see Fig. 1). Since the light reflectance varies with the concentrations of oxy- and deoxyhemoglobin (HbO_2 and Hbr respectively) induced by the hemodynamic response to the neuronal activity, the detection of stimulation related OIS can be used for functional brain-mapping.

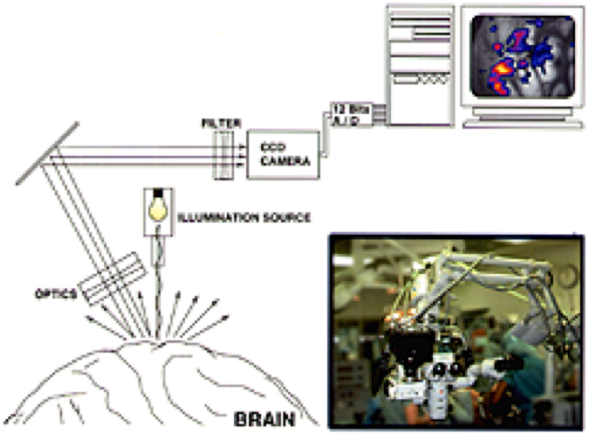

Figure 1: Schematic representation of a typical intraoperative OIS setup. [taken from Ref. [14]]

In this report, we describe the statistical detection tool based on the OIS technique we have developed. This tool is devoted to work in an intraoperative environment in order to guide the neurosurgeons during the brain surgery or to locate spatially the epilepsy. In this document, we focus mainly on the detection of stimulation related neuronal activities. Nevertheless, the tool is adapted to the epilepsy or other neuronal activities detection. We first remind the basic concepts of the OIS technique and the properties of the expected signals in Sec. 2. Then, the detection methods are described in Sec. 3. Finally, we present the user interface of our tool in Sec. 4 and we conclude with a summary of the obtained results and a discussion of the possible improvements in Sec. 5.

2 Introduction

In this section, we present the basics of the OIS technique discussing first the Beer-Lamber law (Sec. 2.1) which describes the relation between the hemoglobin concentrations and the light absorption, then we show typical observed optical signals (Sec. 2.2) and the related linear model (Sec. 2.3) we can use for their prediction. Finally, we briefly remind the acquisition protocol (Sec. 2.4) and how we modelize artificial data sets for the validation of our detection processes (Sec. 2.5).

2.1 Beer-Lambert

The OIS technique is based on the Beer-Lambert law which modelizes the light absorption in a liquid. According to this law and for a monochromatic light of wavelength λ, a small

local temporal variation of oxy- and deoxyhemoglobin concentrations ($\Delta[\mathrm{HbO_2}](\mathbf{r},t)$ and[1] $\Delta[\mathrm{Hbr}](\mathbf{r},t)$ respectively) induces a linearly dependent variation of the reflected light intensity $\Delta I^\lambda(\mathbf{r},t)$, i.e. [2]

$$\frac{\Delta I^\lambda(\mathbf{r},t)}{I_0^\lambda(\mathbf{r})} \propto -\epsilon^\lambda_{\mathrm{HbO_2}} \cdot \Delta[\mathrm{HbO_2}](\mathbf{r},t) - \epsilon^\lambda_{\mathrm{Hbr}} \cdot \Delta[\mathrm{Hbr}](\mathbf{r},t) \tag{1}$$

where $I_0^\lambda(\mathbf{r})$ is the light reflectance at rest. $\epsilon^\lambda_{\mathrm{HbO_2}}$ and $\epsilon^\lambda_{\mathrm{Hbr}}$ are the absorbance coefficients of $\mathrm{HbO_2}$ and Hbr, respectively. These show a strong wavelength dependence (see Fig. 2).

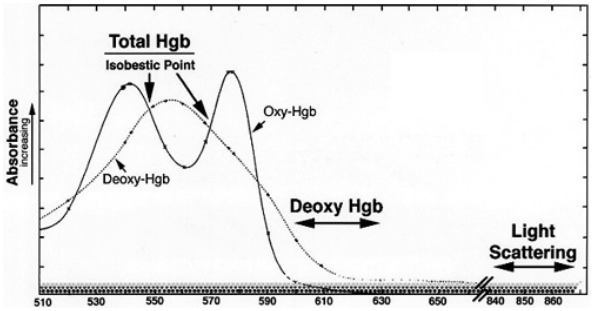

Figure 2: Wavelength λ (in (nm)) dependence of the absorbance coefficients of the oxy- and deoxyhemoglobin ($\epsilon^\lambda_{\mathrm{HbO_2}}$ and $\epsilon^\lambda_{\mathrm{Hbr}}$ respectively). [taken from Ref. [14]]

Following Eq. (1) and Fig. 2, depending on the wavelengths selected by the bandpass filter mounted beneath the CCD camera, the variations of the recorded intensity measure different linear combinations of hemoglobin concentration changes. The two most interesting light filtering are :

- at the isobestic points 550 or 570 nm for which $\epsilon^\lambda_{\mathrm{HbO_2}} = \epsilon^\lambda_{\mathrm{Hbr}}$. In this case the variation of light intensity

$$\frac{\Delta I^\lambda(\mathbf{r},t)}{I_0^\lambda(\mathbf{r})} \propto -\left(\Delta[\mathrm{HbO_2}](\mathbf{r},t) + \Delta[\mathrm{Hbr}](\mathbf{r},t)\right) \tag{2}$$

  measures the the total hemoglobin concentration variation $\Delta[\mathrm{HbO_2}](\mathbf{r},t)+\Delta[\mathrm{Hbr}](\mathbf{r},t) = \Delta[\mathrm{Hbt}](\mathbf{r},t)$.

- above 610 nm, $\epsilon^\lambda_{\mathrm{HbO_2}} \ll \epsilon^\lambda_{\mathrm{Hbr}}$, then the variation of light intensity

$$\frac{\Delta I^\lambda(\mathbf{r},t)}{I_0^\lambda(\mathbf{r})} \propto -\Delta[\mathrm{Hbr}](\mathbf{r},t) \tag{3}$$

  measures mainly the variation of deoxyhemoglobin concentration $\Delta[\mathrm{Hbr}](\mathbf{r},t)$.

2.2 Typical signals

In order to illustrate these two cases, Fig. 3 shows typical optical signals $\Delta I^\lambda(t)/I_0^\lambda$ measured at $\lambda = 550$ nm and 610 nm in a rat model after a 2 s whisker stimulus. These two signals are analogous to the regional cerebral blood flow (rCBF) and the blood oxygen level dependent signal (BOLD) measured in functional magnetic resonance imaging (fMRI) [7]. In effect, an

[1] t stands for the discrete time at which the images are recorded and the vector $\mathbf{r}$ locates the pixels of each recorded image.

[2] The symbol "$\propto$" means "proportional to".

increase in the blood flow follows the neuronal activation to insure the supply in oxygen of the neurons. It results in an increase of the total hemoglobin concentration which leads to a decreasing of the light reflectance intensity at $\lambda = 550$ nm. The blood flow variations being slightly delayed from the neuronal activity, the concentration of deoxyhemoglobin first increases due to the neurons supply in oxygen before being extracted from tissues when the blood flow increases. This results in an initial dip followed by an stronger increase in the light intensity measured at $\lambda = 610$ nm. Although the initial dip of the optical signal at $\lambda = 610$ nm induced by the early increase in deoxyhemoglobin is expected to give the strongest correlation with the neuronal activity [14] (because directly related to the oxygen consumption of the activated neurons), both signals can be used for detecting neuronal activation. In this work, we use a bandpass filter centered at $\lambda = 610$ nm to focus on the deoxyhemoglobin concentration changes.

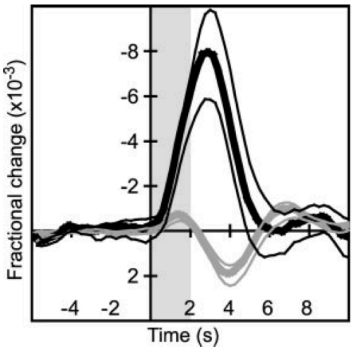

Figure 3: Typical temporal evolution of the optical signals $\Delta I^\lambda(t)/I_0^\lambda$ in a rat model after a 2 s whisker stimulus (gray area) measured at an isobestic point $\lambda = 550$ nm (thick black line) and 610 nm (thick gray line). Thin lines correspond to the error margins. [taken from Ref. [17]]

2.3 Linear response

In order to correctly detect stimuli related neuronal excitations with the OIS technique, it is important to predict as best as possible the light reflection variations $\Delta I^\lambda(\mathbf{r}, t)$ induced by a given stimulus $h(\mathbf{r}, t)$. Although several models of the hemodynamic response such as the balloon model [7] have been developed for the fMRI interpretation, we apply in this work a more experimental model based on a linear response method. Similarly to Ref. [3] for the fMRI, we assume that the temporal variation of the light reflection depends linearly on the time evolution of the stimulus, i.e.[3]

$$\frac{\Delta I^\lambda(\mathbf{r}, t)}{I_0^\lambda(\mathbf{r})} \propto h(\mathbf{r}, t) \star r^\lambda(t) \tag{4}$$

with $r^\lambda(t)$ is the impulsional response of the OIS at the measured light wavelength λ. In this work we consider the experimentally measured impulsional response from Ref. [4] induced by a very short 1 s whisker stimulus in a rat model (see Fig. 4). A comparison between the prediction of the linear response and the OIS signal measured after four periodic 1 s stimuli is shown in Fig. 4.a. As you see in this figure, although the predicted intensity is very close

[3]The symbol "$\star$" means convolution product i.e. $(f \star g)(t) = \int \mathrm{d}\tau\ f(t-\tau)\ g(\tau)$ for continuous functions $f(t)$, $g(t)$ $(t \in \mathbb{R})$ and $(f \star g)_i = \sum_j f_{i-j}\ g_j$ for discrete data sets $f_i = f(t_i)$, $g_i = g(t_i)$ $(i \in \mathbb{Z})$.

to that measured, the linear response overestimates slightly the OIS signal. This effect is probably due to the neuronal adaptation which is neglected by the linear response [3].

In the Fourier basis, the linear response becomes a simple multiplication between the impulsional response and the stimulus, i.e. [4]

$$\frac{\Delta \hat{I}^{\lambda}(\mathbf{r},\nu)}{I_0^{\lambda}(\mathbf{r})} \propto \hat{h}(\mathbf{r},\nu)\cdot\hat{r}^{\lambda}(\nu). \tag{5}$$

Convolved with the stimulus, the impulsional response $\hat{r}^{\lambda}(\nu)$ behaves like a lowpass filter with peaks located at the frequency of its pseudo period (see Fig. 4.b). This implies that the predictions using the linear response have principally low frequency components and it suggests that the high frequency signals in the measured OIS are mainly due to the noise. These can be observed in the predicted and the measured spectra of the four stimuli OIS in Fig. 4.b which shows mainly low frequency components in the same support as the impulsional response. The additional peaks in the four stimuli OIS originate from the Fourier transform of the stimuli $\hat{h}(\nu)$.

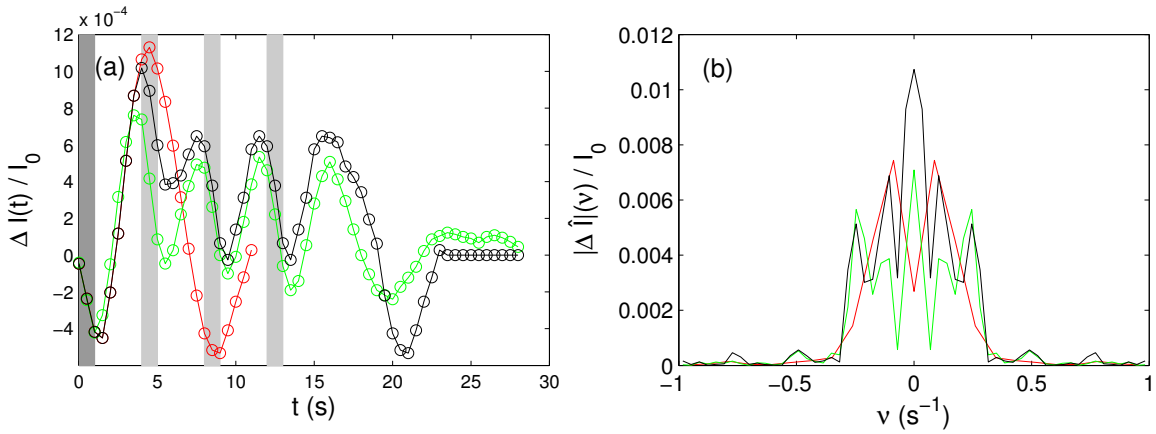

Figure 4: (a) Comparison between the variation of the OIS, $\Delta I^{\lambda}(t)/I_0^{\lambda}$, from Ref. [4] measured at $\lambda = 635$ nm in a rat model after a 1 s whisker stimulus (in red), four repeated 1 s whisker stimuli (in green)). The linear response prediction of the four 1 s whisker stimuli OIS computed with Eq. (4) and the 1 s whisker stimulus (in red) considered as the impulsional response $r^{\lambda}(t)$ is plotted in black. The dark gray area represents the first 1 s whisker stimulus and the light gray areas are the three next stimuli. (b) Absolute value of the discrete Fourier transform of the quantities shown in (a) with the same color code.

In the following, we use the linear response to modelize the artificial data (see Sec. 2.5) for testing our activity detection methods. On the contrary, in the detection process, the modelized neuronal activity in the linear model (see Sec.3.1) is simply the stimulus $h(t)$ (i.e. $r^{\lambda}(t) = \delta(t)$).

2.4 Data acquisition

In this work, the data acquisition of the light reflectance filtered at $\lambda = 610$ nm is performed with a CCD camera with resolution 496×658 pixels. For decreasing the computation time, we

[4]The Fourier transform $\hat{f}(\nu)$ of a function $f(t)$ $(\nu, t \in \mathbb{R})$ is defined as $\hat{f}(\nu) = \int \mathrm{d}t\ f(t)\ e^{-i2\pi\nu t}$ and as $\hat{f}_k = \sum_j f_j\ e^{-i2\pi j\nu_k}$ for the discrete Fourier transform $\hat{f}_k = \hat{f}(\nu_k) = \hat{f}(k/(N\Delta t))$ for a set of N_t data $f_j = f(t_j) = f(j\Delta t)$ $(j,k = 0..N_t - 1)$.

reduce the spatial resolution by two in the two directions averaging the measured intensity over the 4 neighboring pixels. For the detection of stimulation related neuronal activity, the patient receives periodically an electric stimulation on the median nerve of its wrist. The chosen acquisition protocol consists in 4 repeated blocks of 48 s composed of 24 s of stimulation followed by 24 s of rest (see Fig. 5). The duration of the stimulus and the rest should be long enough in order to minimize the transitory effects which are ~ 12 s long (see the impulsional response in Fig. 4.a). Thereby the stimulus has Fourier components in the support of the impulsional response (see Fig. 4.b). In addition, the acquisition rate ν_a should be high enough to include all the details of the hemodynamique response, i.e. $\nu_a \gtrsim 0.5$ s^{-1} (see Fig. 4.b). In this work, we chose $\nu_a = 2$ s^{-1}, i.e. a picture is recorded every discrete time $t_i = i\Delta t$ with $i = 1..N_t$ ($N_t = 384$ and $\Delta t = 0.5$ s) synchronized with the stimulus.

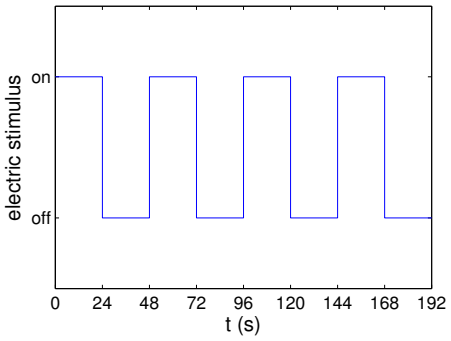

Figure 5: Temporal evolution of the electric stimulus.

2.5 Artificial data

In order to test the detection methods presented in the next section, we need artificial sets of data in which the activation areas are known. Furthermore the characteristics of these simulated data must modelize as well as possible those of the original data. Thus, we start the data modelization with the time average of the original data set ("average" picture in Fig. 7). On the top of the cortical area, we add 8 activated zones (2 for each radii 2.5, 5, 10, and 15 pixels). In order to smooth their boundaries, these activated zones are convolved with a gaussian spatial filter with a standard deviation of 2 pixels ("activated zones" picture in Fig. 7). Applying the linear response on the temporal evolution of the electric stimulus shown in Fig. 5 (Sec. 2.3) we modelize the reflexion intensity variation $\Delta I(\mathbf{r}, t)/I_0(\mathbf{r})$ in each pixel of the activated zones ("activity" picture in Fig. 7). The activation amplitude of $\Delta I(\mathbf{r}, t)/I_0(\mathbf{r})$ is chosen to be 0.01 (after the transition response). This corresponds to the typical order of magnitude of the OIS measured in human cortices [16]. Afterward the obtained temporal series are moved according to the displacement field (multiplied by 2) extracted from the registration of the original data (see Sec. 3.2). Finally, we add a gaussian noise with a standard deviation of[5] 200 in agreement with the noise measured in the original data. This computational scheme of the artificial data is pictured in Fig. 6.

[5]The total amplitude of the recorded pictures is $2^{14} = 16384$.

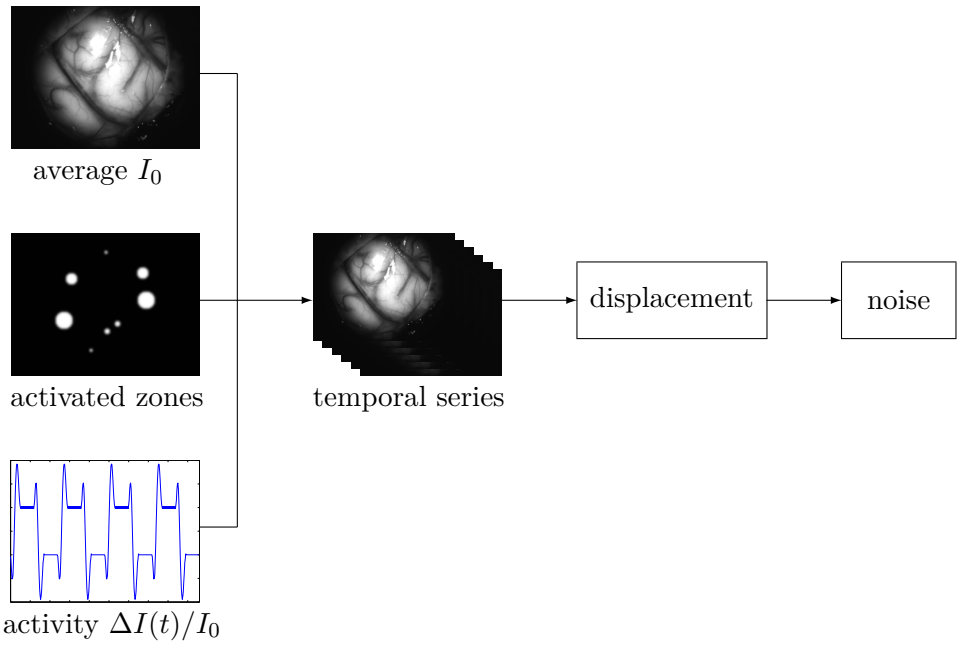

Figure 6: Diagrammatic representation of the artificial data computation. The modelized "activity" $\Delta I(t)/I_0$ is applied on the "average" data in the chosen "activated zones" located inside the cortical area. The "temporal series" generated in this way is then moved applying the displacement field and noised.

3 Detection methods

Although the cornerstone of our stimulus related neuronal activity detection is provided by the general linear model (GLM) [5] discussed in Sec. 3.1, many important preprocessing steps are necessary to improve the quality of the data and the detection precision. Before discussing how these precomputational steps are combined, we briefly describe each of them in the following.

Registration The data acquisition taking few minutes, the brain is free to move during that time due to the breathing or the heartbeat. Thus, in order to match each picture with the others, a registration step described in Sec. 3.2 is necessary for decreasing the movement related noise.

Glare detection (GD) The refraction index of the cortical being different from that of the air, it generates interface reflexions which pollute the OIS related reflexion discussed in Sec. 2.1. As these glares are uncorrelated with the stimulus they mainly add noise to the measured data. Furthermore, these can be strong when the reflexion angle is close to the light incident angle. It is then important to detect the glare areas in order to omit them from the neuronal activity detection process. The details of the irrelevant (glare and outside the cortical) area detection technique is given in Sec. 3.3.

Spatial filtering (SF) and Time filtering (TF) In order to increase the signal-to-noise ratio, spatial and time filtering described in Sec. 3.4 and Sec. 3.5.1 can be performed as precomputational steps. In addition these filters will impose the correlations in the data which are important to be known to adapt the statistical test.

Time whitening (TW) The residual movement of the cortex after the registration and the slow hemodynamic response gives rise to time correlations in the measured OIS. For a correct use of the statistical test, we can perform a time whitening precomputational step described in Sec. 3.5.2 which aims to decorrelate the data.

Wavelet transform (DWT) Since the hemodynamic response spreads out around the neuronal activity, the OIS signal can be strongly spatially correlated. The spatial extent of these correlations being not uniform, the sensitivity of the statistical detection tool must be independent on the size of the neuronal activity. One possible way to tackle this problem consists in decomposing the spatial components of the data in a multiscale wavelet basis [11,12]. In this basis the recorded data become uncorrelated and can then be treated as independent variables in the statistical test (see Sec. 3.6).

As shown in Fig. 7, by combining these steps we implement two computational processes; the "standard process" in which all the precomputational steps are performed in the spatial basis and the "wavelet process" which includes the wavelet decomposition in order to decorrelate the data.

Standard process:

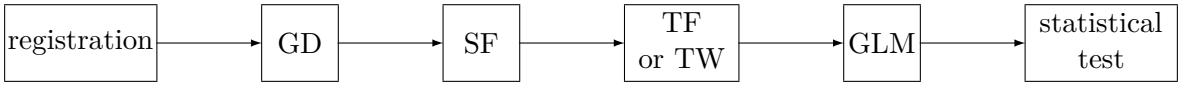

Wavelet process:

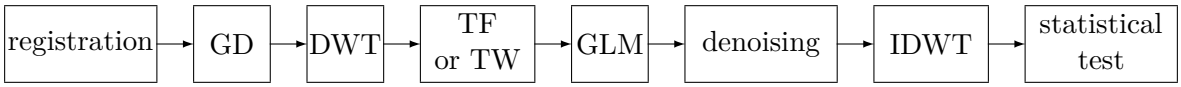

Figure 7: Diagrammatic representation of the two possible processes (standard process : process in the spatial basis, wavelet process : process including the wavelet decomposition). The abbreviations employed in this diagram are GD: glare detection, SF: spatial filtering, TF: time filtering, TW: time whitening, GLM: general linear model, DWT: discrete wavelet transform and IDWT: inverse discrete wavelet transform.

In the next sections, we first introduce the linear model and the statistical test that we perform for the neuronal activity detection. Then we present each precomputational steps listed above in details following the standard process (in Fig. 7). To illustrate the effect of each step, an analysis of the statistical test performed on two original (Sec. 2.4) and artificial (Sec. 2.5) sets of data are presented. Finally we describe the wavelet process (in Fig. 7).

3.1 General linear model (GLM)

The detection of the neuronal activity is based on the well known general linear model [2, 9] which has been intensively used to interpret fMRI [5]. In this section, we remind the main idea of this method.

Writing the time evolution of the modelized intensity[6] in a vector[7] $\mathbf{I} \in \mathcal{M}_{N_t}(\mathbb{R})$ (i.e. the

[6] In this section we omit the position vector $\mathbf{r}$ of the measured intensity.

[7] $\mathcal{M}_{a,b}(\mathbb{R})$ stands for a matrix of size $a \times b$ with real coefficients. When $b = 1$, the b index is omitted (i.e. $\mathcal{M}_a(\mathbb{R})$ stands for a vector of size b).

i^{nd} component $I_i = I(t_i)$ with $i = 1..N_t$), the linear assumption of the GLM is

$$\mathbf{I} = \mathbf{G}\boldsymbol{\beta} + \mathbf{e} \tag{6}$$

with $\mathbf{G} \in \mathcal{M}_{N_t,m}(\mathbb{R})$ is a matrix of rank m with its columns filled by the m regressors of the model, the vector $\boldsymbol{\beta} \in \mathcal{M}_m(\mathbb{R})$ contains the parameters of the model, and $\mathbf{e} \in \mathcal{M}_{N_t}(\mathbb{R})$ is a random vector assumed to follow a multivariate normal distribution[8] $\mathbf{e} \sim \mathcal{N}(0, \sigma^2\boldsymbol{\Omega})$ with $\boldsymbol{\Omega} \in \mathcal{M}_{N_t,N_t}(\mathbb{R})$ is the symmetric and positive defined covariance matrix of $\mathbf{e}/\sigma$.

The regressors included in $\mathbf{G}$ should reproduce the expected features of the modelized intensity $\mathbf{I}$ in Eq. (6). In the following we will consider that the first regressor corresponds to the stimulation induced OIS intensity (Sec. 2.3) which will be completed by some possible corrections. For example, as the measurement is relatively long, we have to include regressors which reproduce the slow variations of the light exposure. These are modelized by a 4^{th} order polynomial (the related five regressors are $\mathbf{t}^{(j)}$ with components $t_i^{(j)} = t_i^j$ and $j = 0..4$, $i = 1..N_t$) and have the effect of a high pass filter. In addition, the two main sources of motion being the heartbeat and the breathing, their related components with frequency ν_h and ν_r, respectively, should be also included in the model. These frequencies are computed from a Fourier analysis of the time evolution of the global intensity. Therefore, we add the four regressors $\mathbf{s}^{(h,r)}$ and $\mathbf{c}^{(h,r)}$ with components $s_i^{(h,r)} = \sin(2\pi\nu_{h,r}t_i)$ and $c_i^{(h,r)} = \cos(2\pi\nu_{h,r}t_i)$ for $i = 1..N_t$, respectively.

Usually, σ is unknown and we want to infer the parameters $\boldsymbol{\beta}$ of the model (6) according to a set of measured OIS data $\tilde{\mathbf{I}}$. Thus we use the generalized least square estimator of[9] $\boldsymbol{\beta}$:

$$\tilde{\boldsymbol{\beta}} = \left(\mathbf{G}'\boldsymbol{\Omega}^{-1}\mathbf{G}\right)^{-1}\mathbf{G}'\boldsymbol{\Omega}^{-1}\tilde{\mathbf{I}} \quad \text{with} \quad \text{Var}(\tilde{\boldsymbol{\beta}}) = \sigma^2\left(\mathbf{G}'\boldsymbol{\Omega}^{-1}\mathbf{G}\right)^{-1}. \tag{7}$$

and the unbiased estimator of σ^2:

$$\tilde{\sigma}^2 = \frac{\left(\tilde{\mathbf{I}} - \mathbf{G}\tilde{\boldsymbol{\beta}}\right)'\boldsymbol{\Omega}^{-1}\left(\tilde{\mathbf{I}} - \mathbf{G}\tilde{\boldsymbol{\beta}}\right)}{N_t - m} \tag{8}$$

Hence, the statistical test of the null hypothesis $H_0 : \beta_1 = 0$ (no stimulation related OIS) is performed on the quantity

$$T = \frac{\mathbf{c}'\tilde{\boldsymbol{\beta}}}{\sqrt{\tilde{\sigma}^2\mathbf{c}'\left(\mathbf{G}'\boldsymbol{\Omega}^{-1}\mathbf{G}\right)^{-1}\mathbf{c}}} \quad \text{with} \quad \mathbf{c}' = [1, \underbrace{0, \cdots, 0}_{m-1}]. \tag{9}$$

If the null hypothesis and all the assumptions of the general linear model are verified, $T \sim t_{N_t-m}$ i.e. T follows the Student's t-distribution with $N_t - m$ degrees of freedom[10]. The rejection of the null hypothesis is therefore interpreted in our case as the presence of a neuronal excitation. The rejection threshold t_α of the statistical test is imposed by fixing the probability α of rejecting the null hypothesis H_0 when it is true (type I error[11] or false positive) i.e.

$$\text{rejection when} \begin{cases} T > t_\alpha & \text{with } P(T > t_\alpha) = \alpha \quad \text{(one-tailed test)} \\ |T| > t_\alpha & \text{with } P(|T| > t_\alpha) = \alpha \quad \text{(two-tailed test)} \end{cases}. \tag{10}$$

[8] The density of the multivariate normal distribution is given by the function $f_{\mathbf{X}}(\mathbf{x}) = \frac{\exp\left(-\frac{\mathbf{x}'\boldsymbol{\Omega}^{-1}\mathbf{x}}{2\sigma^2}\right)}{(2\pi)^{N_t/2}\sigma^{N_t}\det(\boldsymbol{\Omega})^{1/2}}$.

[9] The symbol " ′ " stands for the transposition and "Var" is the variance.

[10] The density of the Student's t-distribution with N degrees of freedom is given by the function $f_X(x) = \frac{\Gamma\left(\frac{N+1}{2}\right)}{\sqrt{N\pi}\Gamma\left(\frac{N}{2}\right)}\left(1 + \frac{x^2}{N}\right)^{-\frac{N+1}{2}}$.

[11] The acceptation of the null hypothesis H_0 when it is false is called type II error.

The statistical threshold t_α is computed according to the Stutent's distribution t-distribution with $N_t - m$ degrees of freedom. The one-tailed test is performed when only a positive excitation is expected whereas we use the two-tailed test when the sign of the excitation does not matter.

Typically $\alpha = 0.05$ is chosen, but for images with a large number of pixels $N_p = N_x \cdot N_y$, we prefer to fix a more conservative threshold fixing the false positive probability of a pixel over all i.e.[12] $P(\max_{\mathbf{r}} T(\mathbf{r}) > t_\alpha) = \alpha$ with $\max_{\mathbf{r}} T(\mathbf{r})$ is the maximal T value over all the pixels. Therefore performing the statistical test (10) on each pixel (located in $\mathbf{r}$) separately, α can be rectified by $\alpha \to \alpha/N_p$ in the threshold t_α determination (10) according to the Bonferonni inequality

$$P(\max_{\mathbf{r}} T(\mathbf{r}) > t_\alpha) \leq N_p \; P(T(\mathbf{r}) > t_\alpha). \tag{11}$$

As we will see in Sec. 3.4, the Bonferonni correction can be improved when the data are spatially filtered thanks to the random field theory.

Finally, the time correlations expressed in the covariance matrix $\mathbf{\Omega}$ which originate from many unknown effects such as the long time hemodynamic response or the residual cortical movement (even after the registration) are difficult to estimate. Although we will see in Sec. 3.5.2 how we can modelize these correlations through a 1^{st} order autoregressive model, we first assume the simplified case[13] $\mathbf{\Omega} = \mathbb{I}_{N_t}$ i.e. the data are uncorrelated in time.

3.2 Registration

During the acquisition of the data, the observed part of the cortex is free to move principally owing to the heartbeat and the breathing. Thus, in order to minimize the motion related noise, a registration precomputational step is necessary. The movement of the brain being not uniform, it is important to implement a deformable registration process which can take into account all the possible non-rigid cortical deformations. In this work, we choose the "demons" algorithm [18] included in the ITK library [10]. As we will see below, once it is well parametrized, this algorithm is very efficient for matching cortical pictures when they are slightly deformed.

The main idea of this algorithm is to compute a deformation field $\mathbf{d}(\mathbf{r})$ allowing to match the contour lines of a deformable image $m(\mathbf{r} + \mathbf{d}(\mathbf{r}))$ with those of a static image $s(\mathbf{r})$ (see Fig. 8). Following this goal, the deformation field is computed iteratively by considering the action of local forces "demons" acting on each pixel of the static image and pushing the deformable image in the direction normal to its contour lines. Starting with an initial displacement field $d^0(\mathbf{r})$, the n^{nd} recursive step for the computation of the displacement field is given by

$$\mathbf{d}^{(n)}(\mathbf{r}) = \mathbf{d}^{(n-1)}(\mathbf{r}) - \underbrace{\frac{m\left(\mathbf{r} + \mathbf{d}^{(n-1)}(\mathbf{r})\right) - s(\mathbf{r})}{||\nabla s(\mathbf{r})||^2 + \left[m\left(\mathbf{r} + \mathbf{d}^{(n-1)}(\mathbf{r})\right) - s(\mathbf{r})\right]^2} \nabla s(\mathbf{r})}_{=\Delta \mathbf{d}^{(n)}(\mathbf{r})}. \tag{12}$$

Thereby, the small correction to the displacement field at the $n^{(\text{th})}$ iteration step $\Delta\mathbf{d}^{(n)}(\mathbf{r})$ is parallel to $\nabla s(\mathbf{r})$ i.e. it is normal to the contour lines of $s(\mathbf{r})$. Furthermore the amplitude of the correction matches the supposed distance between the two images except close to the convergence of the algorithm which requires a correction of the denominator for avoiding a

[12] $P(\{\max_{\mathbf{r}} T(\mathbf{r}) > t_\alpha\} \cup \{\min_{\mathbf{r}} T(\mathbf{r}) < -t_\alpha\}) = \alpha$ for a two-tailed test.

[13] $\mathbb{I}_{N_t} \in \mathcal{M}_{N_t,N_t}(\mathbb{R})$ is the identity matrix of size $N_t \times N_t$.

divergence of (12) when $m - s$ is small. The figure 8 illustrates the iteration step (12) where the $\Delta\mathbf{d}^{(n)}(\mathbf{r})$ are represented by "demons" pushing the contour lines of the deformed image toward those of the static image. In this work, the static image is chosen as the time average of the data while the deformable images are all the recored images of the time series.

Additionally, in order to make the registration algorithm more stable and to adapt its sensitivity to the length scale of the expected cortical deformations, the computed deformation field is smoothed with a gaussian filter between each iteration step. This is equivalent to impose an elastic-like behavior to the deformation. The standard deviation σ_f of the gaussian filter fixes the length scale below which the deformation field remains smooth. As a result, the registration algorithm with a too small σ_f will overestimate the local variations of the deformation field and then add registration artifact to the detection process. Conversely, some important local deformations can be neglected when setting a too large σ_f. These effects will be analyzed below.

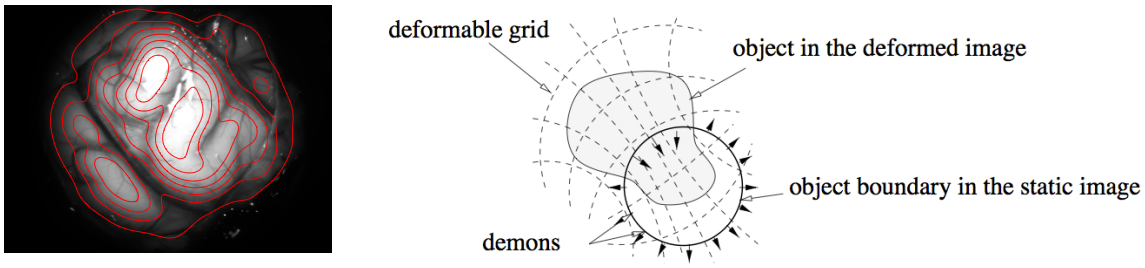

Figure 8: (left): The contour lines (in red) of the time average of the data (grayscale image) once a gaussian filter with $\sigma_f = 8$ pixels is applied on the data. (right): Sketch of the iteration step (12). The "objects" are the contour lines in both images and the "demons" are the local forces on the static image pushing the deformed image. [taken from Ref. [18]]

In order to make the algorithm faster and more robust, we adopt a multi resolution scheme sketched in Fig. 9. The displacement field is first computed in a coarse scale and used to initialize the registration algorithm at the next finer level which becomes then faster to converge. As a result, the number of iterations necessary for the algorithm convergence decreases from ≈ 30 (for the algorithm without a multi resolution scheme) to $\lesssim 10$ in each scale (for a 3 scales multi-resolution algorithm, each scale being 2 times finer than the next one).

As the neuronal activity detection is performed in an intraoperative environment, its computation should be as fast as possible. The registration of each recorded image being the most time consuming step, it must be parallelized to decrease the total computation time. In this work, we parallelize each registration using the openMP library [13] on a shared-memory multiprocessor computer. A performance comparison between the registrations performed with the openMP parallelization and the parallelization implemented in the ITK library itself (both with and without multi-resolution algorithm) is shown in Fig. 10. As expected, the multi-resolution registration algorithm is (≈ 2 times) faster than its single scale implementation. Moreover, the openMP parallelization divides the computation time almost exactly by the number of involved processors because it distributes each registration separately on all the processors. In opposite, the ITK library parallelizing each image registration itself, the ITK parallelization becomes less efficient when the number of involved processors is important.

To illustrate the effects of the registration process on the computed T values and the related neuronal activity detection, we show in Figs. 12 and 13 a false color representation and the histogram of the local $T(\mathbf{r})$ values directly computed after the registration (Fig. 11)

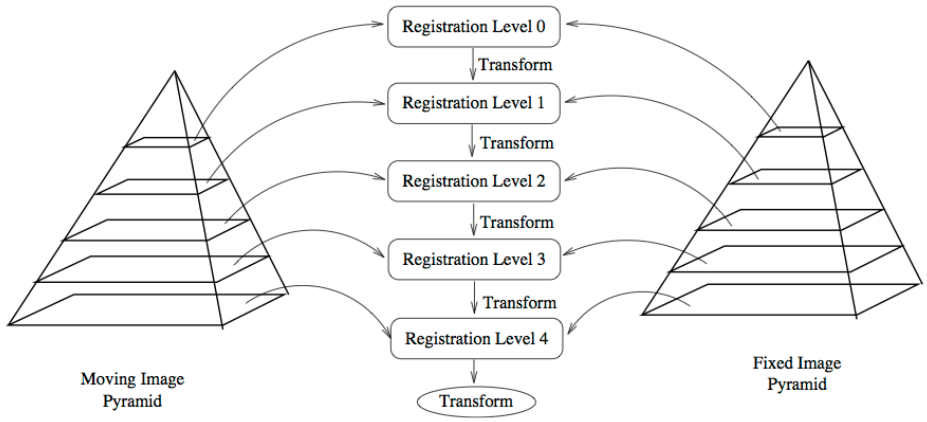

Figure 9: Conceptual representation of the multi-resolution registration process. [taken from Ref. [10]]

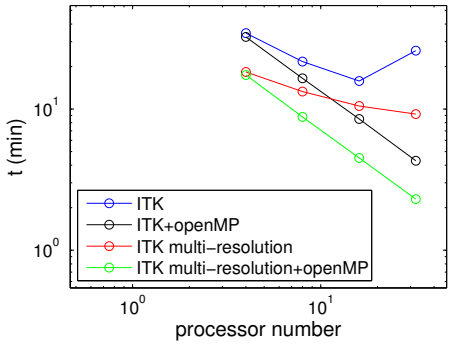

Figure 10: Scaling of the registration computation time versus the number of involved processors. ITK: registration with the ITK parallelization without the multi-resolution algorithm. ITK+openMP: registration with the openMP parallelization without the multi-resolution algorithm. ITK multi-resolution: registration with the ITK parallelization and the multi-resolution algorithm. ITK multi-resolution+openMP: registration with the openMP parallelization and the multi-resolution algorithm.

for several σ_f on the artificial (Sec. 2.5) and the measured data (Sec. 2.4), respectively.

For the artificial data, as expected the registration algorithm removes a part of the motion related noise[14]. This results in a strong increase in the detection sensitivity (increase in true excitations in Fig. 12). Nevertheless the choice of σ_f remains crucial. As discussed above, a too large σ_f restricts the registration to large scale displacements. Therefore, it can not correctly detects local movements and leads to an increase in type I errors (see the case $\sigma_f = 12$ pixels in[15] Fig. 12)). In opposite, the registration algorithm can wrongly interpret the data when σ_f is too small. For example, some variations of the stimulus related OIS are corrected during the registration process which decreases the detection sensitivity (see the case $\sigma_f = 2$ pixels in Fig. 12). Note that the distribution of the T values of the artificial data

[14]Note that we have compared the difference between the added movement in the artificial data and the displacement field extracted from the registration algorithm. Both are in good agreement for all the σ_f shown in Fig. 12 (comparison not shown here).

[15]The displacement field applied on the artificial data originates from that computed in the registration of the original data with $\sigma_f = 8$ pixels.

is only slightly modified by the registration process and is very similar to that expected i.e. the Student's t-distribution.

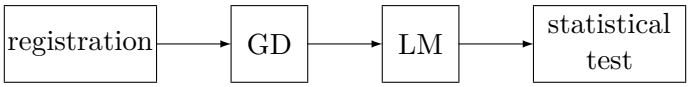

Figure 11: Diagrammatic representation of the computation process restricted to the registration step. We use the same abbreviations as in Fig. 7.

For the analysis of the measured data, we choose $\sigma_f = 8$ pixels. With this filter size, the registration corrects the main part of the brain motion without adding too much interpretation errors. Similarly to the artificial data, the registration decreases the motion related noise. As a result, the distribution of the T values is broadened and recentered, and the detection sensitivity is increased (see Fig. 13).

3.3 Glare detection

As briefly mentionned in Sec. 3, in order to a avoid misleading analysis, the glare areas appearing when the reflected light makes an angle close to the incident light must be eliminated from the neuronal detection process. These glares are easily detected by analysing the time series. In this work, we remove from the neuronal activity detection process the following area:

- the pixels equal or exceeding the maximum intensity of the time averaged data at least once during all the time evolution
- the pixels with very strong peak intensity i.e. when the variation of intensity between two time steps exceed 50% of its original value.

For the same reason, the pixels outside the cortical area must be also omitted from the neuronal activity detection process. These pixels having mainly a small OIS intensity, they are determined by analyzing the histogram of the time averaged data. This histogram peaks at low intensity due to the large number of pixels outside the cortical area. We then evaluate from the upper boundary of the peak an intensity threshold below which the pixels are considered outside the cortical area.

Finally, the total omitted area is dilated with a small circle with a radius of 2 pixels to eliminate the glare boundaries

3.4 Spatial filtering

One way to increase the sensitivity of the neuronal activity detection consists in filtering spatially the recorded pictures once they are registrated. Ideally, if the OIS is spatially independent, filtering the data will smooth the fluctuations and decrease the noise. As a result, we expect an increase in the detection sensitivity. Following this idea, we convolve each recorded picture by a 2D gaussian filter[16]. The key parameter of this filter is the standard deviation σ_s which should be adapted to the neuronal activation size. A too small filter will be inefficient while a very large filter will broaden the detected area and then reduce the

[16] A d-dimensionnal gaussian filter with spatial standard deviation σ_s is given by the function $f(\mathbf{r}) = \frac{e^{-\frac{||\mathbf{r}||^2}{2\sigma_s^2}}}{\left(2\pi\sigma_s^2\right)^{d/2}}$

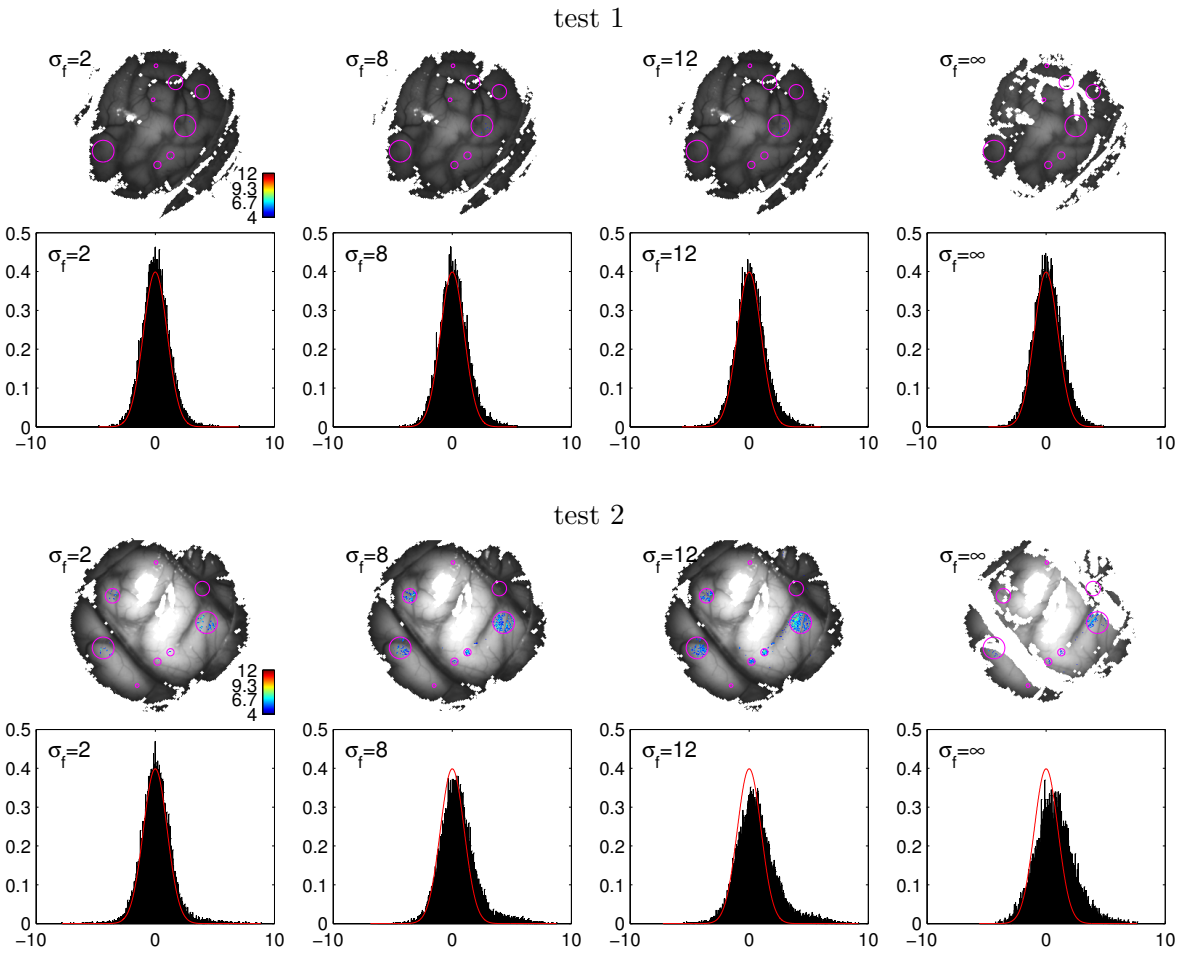

test 1

σ_f (pixel)	2	8	12	∞
true excitations	4	10	13	0
false excitations	0	0	3	0

test 2

σ_f (pixel)	2	8	12	∞
true excitations	132	456	622	147
false excitations	2	34	89	38

Figure 12: Test on two artificially computed data (test 1 and 2) (see Sec. 2.5). Each test includes: (figure above): False color representation of the local $T(\mathbf{r})$ values (Eq. (9)) computed directly after the registration step (see Fig. 11) for $\sigma_f = 2, 8, 12$ pixels and $\sigma_f = \infty$ (no registration) when the null hypothesis H_0 is rejected according to a one-tailed test (Eq. (10)) with $t_\alpha = 4.93$ ($\alpha = 0.05$ and considering the Bonferonni correction). The grayscale image represents the time average of the data and the white area is the omitted irrelevant area (Sec. 3.3). The pink circles locate the boundaries of the artificially added excitations. (figure below): Histogram of the T values included in the relevant area. The red curve represents the expected Student's t-distribution with 374 degrees of freedom. (table): Number of pixels rejecting the null hypothesis inside (true excitations) and outside (false excitations) the added excitations area. The false excitations are equivalent to the errors of type I and 2184 (number of artificially excited pixels) minus the true excitations correspond to the errors of type II.

spatial resolution by a factor of approximately $2\sqrt{2\log 2}\sigma_s$ (the full width at half maximum (FWHM) of the filter).

In addition, when a spatial filtering is performed, the spatial correlations are normalized

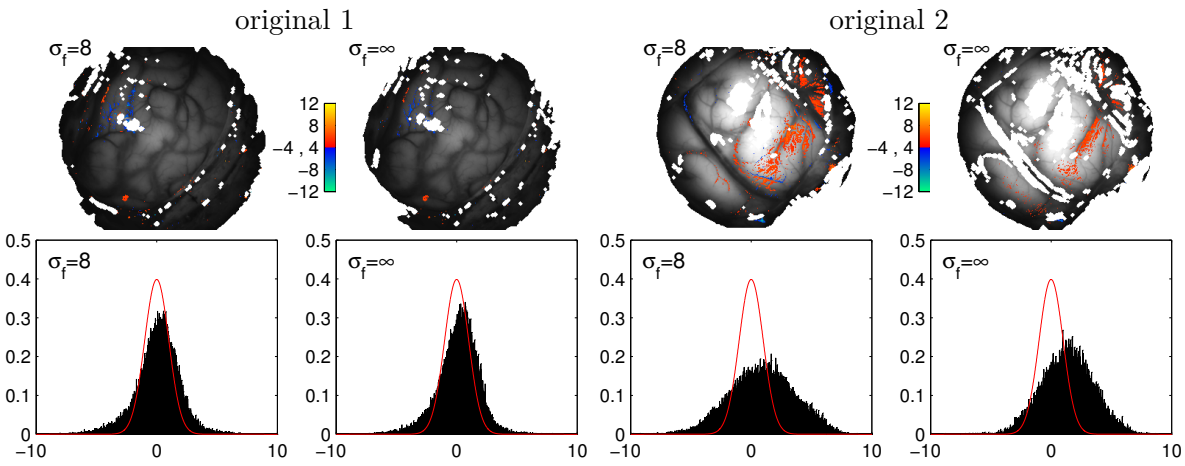

Figure 13: Same results as Fig. 12 but computed with the measured OIS (see Sec. 2.4) for $\sigma_f = 8$ pixels and $\sigma_f = \infty$ (no registration) on two different patients (original 1 and 2) using a two-tailed test with $t_\alpha = 5.07$.

by the filter size and become stronger. In this case, the Bonferonni correction (11) of the detection threshold can become too conservative. A less restrictive statistical test results from the random field theory [1]. It has been demonstrated [21, 22, 25] that the tail probability $P(\max_{\mathbf{r}} T(\mathbf{r}) > t_\alpha)$ of a smoothed random field of Student's variables $T(\mathbf{r})$ (with N degrees of freedom) can be approximated by

$$P(\max_{\mathbf{r}} T(\mathbf{r}) > t_\alpha) \approx \frac{\Gamma\left(\frac{N+1}{2}\right) N_p}{2(2\pi)^{3/2}\left(\frac{N}{2}\right)^{1/2}\Gamma\left(\frac{N}{2}\right)\sigma_s^2}\left(1+\frac{t_\alpha^2}{N}\right)^{-\frac{1}{2(N-1)}}. \tag{13}$$

This expression allows us to compute the threshold t_α for a given probability α. The latter is compared with the Bonferonni threshold in Fig. 14. It shows that for small $\sigma_s \lesssim 2$ pixels, the Bonferonni threshold is less conservative than that extracted from the random field theory. On the contrary, for larger $\sigma_s \gtrsim 2$ pixels the Bonferonni threshold is more conservative. In the following, we will take the optimal statistical threshold chosen as the smaller between the Bonferonni or the random field theory.

To show the effects of the spatial filtering, we present in Figs. 16 and 17, a false color representation and the histogram of the local $T(\mathbf{r})$ values directly computed after the spatial filtering (see the restricted process in Fig. 15)) for several σ_s on the artificial (Sec. 2.5) and the measured data (Sec. 2.4). As expected, the larger the filter is, the more sensitive the neuronal detection is (increase in true excitations with σ_s in the artificial data (Fig. 16)). Nevertheless, the detected area becomes too much broadened when the filter is large (increase in type I errors with σ_s in the artificial data (Fig. 16)). In addition, when the neighbor pixels are correlated in time, the spatial filter can increase these time correlations (see Sec. 3.5.2) and the temporal decorrelation assumption ($\mathbf{\Omega} = \mathbb{I}_{N_t}$) considered up to now becomes strongly violated. As a result the histogram of the T values deviates from the expected Student's t-distribution. This effect slightly present in the artificial data becomes much stronger when considering the original data which have intrinsically stronger time correlations (see Fig. 16). We will discuss in Sec. 3.5 how these time correlations can be taken into account in the detection process.

In the following, we will use $\sigma_s = 2$ pixels which is a compromise between the sensitivity and the type I error increase. Nevertheless this choice is relatively flexible, because it depends

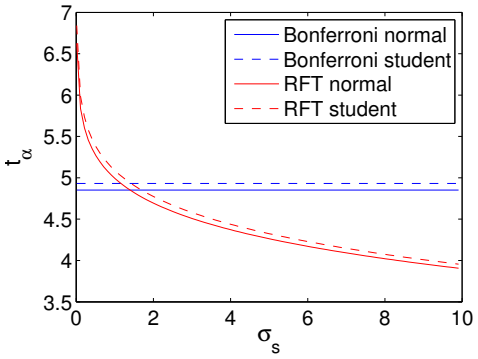

Figure 14: Statistical threshold t_α versus the standard deviation σ_s in (pixel) of the spatial filter computed for a one-tailed test with significance level $\alpha = 0.05$ and considering pictures with $N_p = 248 \times 329$ pixels (half resolution of the camera CCD (see Sec. 2.4)). The threshold computed from the Bonferonni corrected $\alpha \to \alpha/N_p$ and the random field theory (RFT) are shown for the Student's t-statistics with $N = 374$ degrees of freedom (same as for all the statistical tests shown in this report) and $N \to \infty$ (normal statistics).

mainly on the size of the expected neuronal activation area which is usually not known in advance.

Figure 15: Diagrammatic representation of the computation process restricted to the registration followed by the spatial filtering. We use the same abbreviations as in Fig. 7.

3.5 Time corrections

As discussed in Secs. 3 and 3.4, the time correlations can be strong in the measured data. These correlations originate from the slow hemodynamic response, the residual brain motion (after registration) or the not exactly modelized stimulus related OIS (discussed in Sec. 2.3). But, for a correct statistical analysis presented in Sec. 3.1 we should either have uncorrelated data, i.e. $\mathbf{\Omega} = \mathbb{I}_{N_t}$ (as assumed in the previous section), or compute a good approximation of the covariance matrix $\mathbf{\Omega}$.

In the following, we will first describe a method which consists in filtering in time the data to impose the time correlations $\mathbf{\Omega}$. In opposite, the second presented technique uses an autoregressive process to modelize the time correlations $\mathbf{\Omega}$. In both techniques these correlations are assumed equal in all the pixels of the recorded images.

3.5.1 Time filtering

As proposed in Ref. [23], filtering the data in time is a way of fixing the covariance matrix $\mathbf{\Omega}$ while decreasing the noise. To perform this technique, we convolve the time evolution of the data with a gaussian filter. Fixing the standard deviation σ_t, the time filtering cut all the noise with higher frequencies than approximatively $\sqrt{\ln 2}/(\sqrt{2}\pi\sigma_t)$ (the half FWHM of

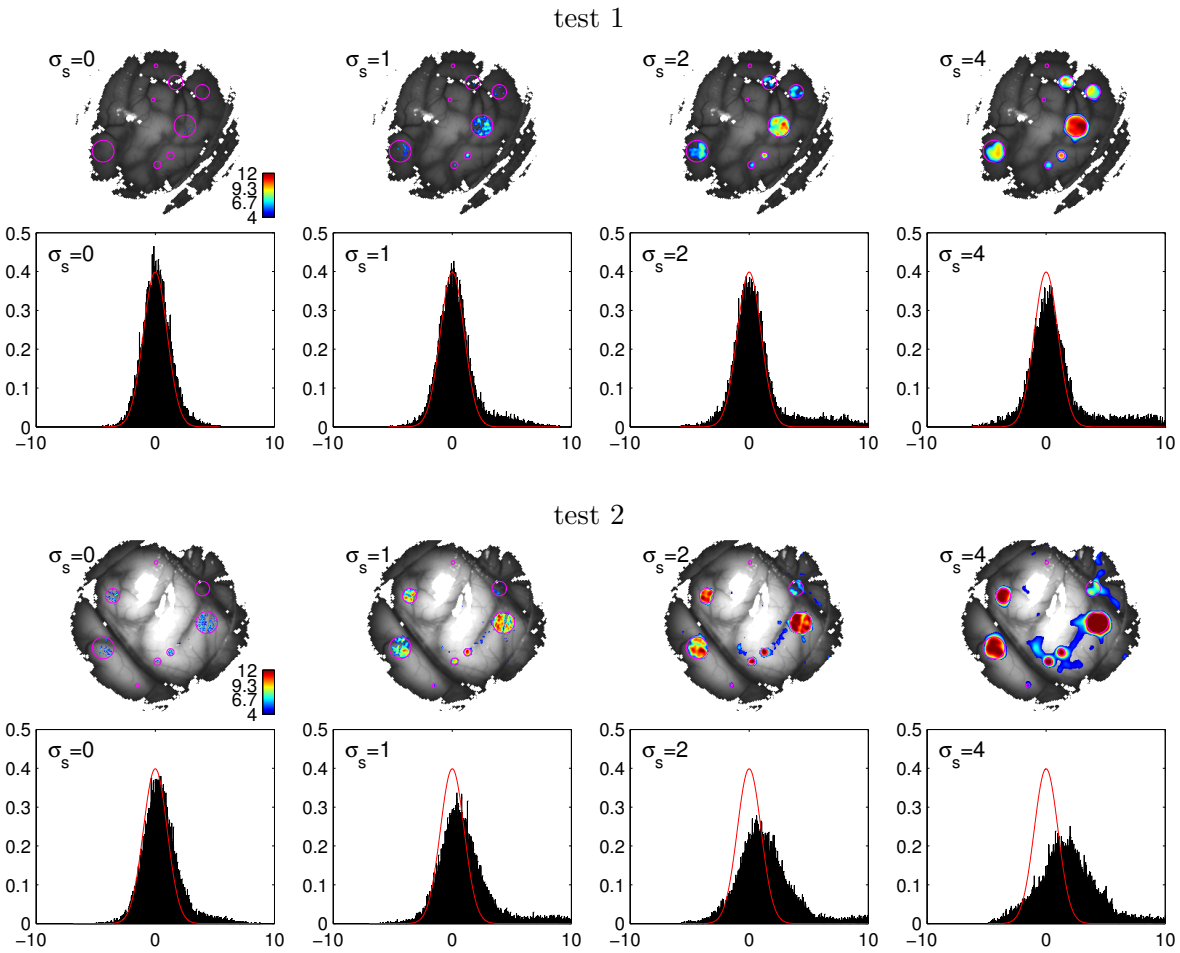

test 1

σ_s (pixel)	0	1	2	4
true excitations	10	611	1584	2028
false excitations	0	2	103	808

test 2

σ_s (pixel)	0	1	2	4
true excitations	456	1561	1932	2109
false excitations	34	307	1152	4136

Figure 16: Test on two artificially computed data (test 1 and 2) (see Sec. 2.5). Each test includes: (figure above): False color representation of the local $T(\mathbf{r})$ values (Eq. (9)) computed directly after the spatial filtering step (see Fig. 15) with $\sigma_s = 0$ (no spatial filtering) and $\sigma_s = 1, 2, 4$ pixels when the null hypothesis H_0 is rejected according to a one-tailed test (Eq. (10)) with $t_\alpha = 4.93, 4.93, 4.77, 4.44$ (for $\sigma_s = 0, 1, 2, 4$ pixel) ($\alpha = 0.05$ and considering the optimal statistical criteria). The grayscale image represents the time average of the data and the white area is the omitted irrelevant area (Sec. 3.3). The pink circles locate the boundaries of the artificially added excitations. (figure below): Histogram of the T values included in the relevant area. The red curve represents the expected Student's t-distribution with 374 degrees of freedom. (table): Number of pixels rejecting the null hypothesis inside (true excitations) and outside (false excitations) the added excitations area. The false excitations are equivalent to the errors of type I and 2184 (number of artificially excited pixels) minus the true excitations correspond to the errors of type II.

the Fourier transform of the gaussian filter[17]). Thus, if we want to keep into account the

[17] A gaussian filter $f(t) = \frac{e^{-\frac{t^2}{2\sigma_t^2}}}{(2\pi)^{1/2}\sigma_t}$ has a Fourier transform $\hat{f}(\nu) = \frac{e^{-\frac{\nu^2}{2\sigma_\nu^2}}}{(2\pi)^{1/2}\sigma_\nu}$ with $\sigma_\nu = \frac{1}{2\pi\sigma_t}$.

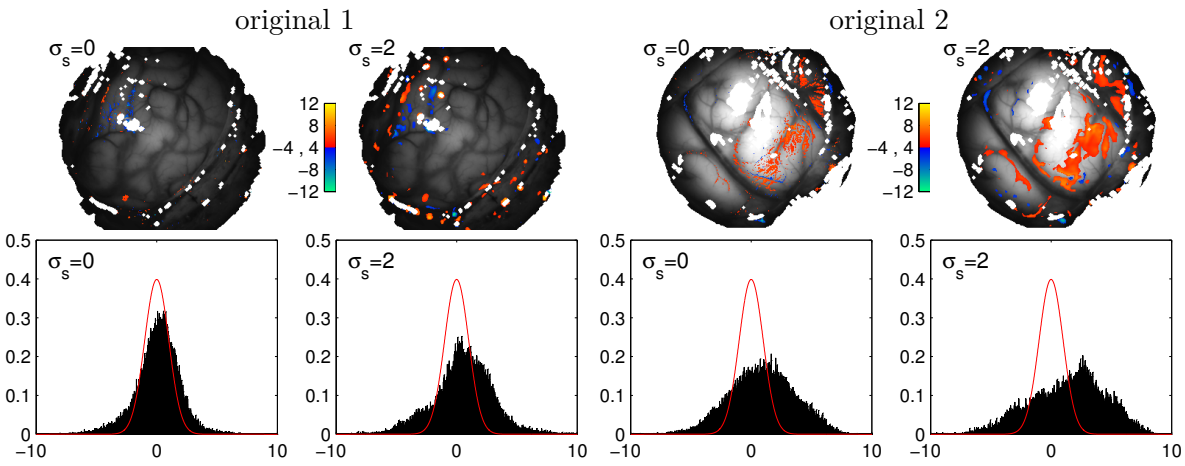

Figure 17: Same results as Fig. 16 but computed with the measured OIS (see Sec. 2.4) for $\sigma_s = 0$ (no spatial filtering) and $\sigma_s = 2$ pixels on two different patients (original 1 and 2) using a two-tailed test with $t_\alpha = 5.07, 4.93$ (for $\sigma_s = 0, 2$ pixel).

details of the hemodynamic response, we must keep $\sigma_t \lesssim 1$ s (see Fig. 4). Nevertheless, in order to assume $\mathbf{\Omega}$ fixed by the time filtering, σ_t must be much larger than the original time correlations of the measured OIS.

Once the data are filtered, we have to adapt the statistical test shown in Sec. 3.1 in order to take into account the imposed correlations. In a matrix form, the time filtering is just a matrix multiplication[18] and Eq. (6) becomes

$$\mathbf{KI} = \mathbf{KG}\boldsymbol{\beta} + \mathbf{e} \tag{14}$$

with $\mathbf{K}$ the matrix associate to the gaussian filter and $\mathbf{e} \sim \mathcal{N}(0, \sigma^2\mathbf{\Omega})$ with $\mathbf{\Omega} \approx \mathbf{KK}'$ (when the temporal correlations of the original OIS are neglected). Instead of using the (best) generalized least square estimator (7) of $\boldsymbol{\beta}$ which requires a very good knowledge of $\mathbf{\Omega}$ for being inverted (it is not the case here), we follow Ref. [23] and consider the unbiased estimator[19]

$$\tilde{\boldsymbol{\beta}}_{tf} = \left(\mathbf{G}^{\star\prime}\mathbf{G}^\star\right)^{-1}\mathbf{G}^{\star\prime}\mathbf{K}\tilde{\mathbf{I}} \quad \text{with} \quad \mathrm{Var}(\tilde{\boldsymbol{\beta}}_{tf}) = \sigma^2\left(\mathbf{G}^{\star\prime}\mathbf{G}^\star\right)^{-1}\mathbf{G}^{\star\prime}\mathbf{K}\mathbf{K}'\mathbf{G}^\star\left(\mathbf{G}^{\star\prime}\mathbf{G}^\star\right)^{-1} \tag{15}$$

and the related unbiased estimator of[20] σ^2:

$$\tilde{\sigma}^2_{tf} = \frac{\left(\mathbf{K}\tilde{\mathbf{I}} - \mathbf{G}^\star\tilde{\boldsymbol{\beta}}_{tf}\right)'\left(\mathbf{K}\tilde{\mathbf{I}} - \mathbf{G}^\star\tilde{\boldsymbol{\beta}}_{tf}\right)}{\mathrm{Tr}(\mathbf{RKK}')} \tag{16}$$

which are computed directly with the filtered data $\mathbf{K}\tilde{\mathbf{I}}$. Hence, the statistical test is performed on the quantity

$$T_{tf} = \frac{\mathbf{c}'\tilde{\boldsymbol{\beta}}_{tf}}{\sqrt{\tilde{\sigma}^2_{tf}\mathbf{c}'\left(\mathbf{G}^{\star\prime}\mathbf{G}^\star\right)^{-1}\mathbf{G}^{\star\prime}\mathbf{K}\mathbf{K}'\mathbf{G}^\star\left(\mathbf{G}^{\star\prime}\mathbf{G}^\star\right)^{-1}\mathbf{c}}}. \tag{17}$$

[18] The convolution of a discrete data set $f_i = f(t_i)$ with a filter $k_i = k(t_i)$ with $i = 1..N_t$ can be written in a matrix form i.e. $\mathbf{Kf}$ with $K_{ij} = k(t_{i-j})$ (in this work we have considered periodic boundaries, i.e. $k(t_{i-j}) = k(t_{N_t+i-j})$ if $i \leq j$).

[19] $\mathbf{G}^\star$ stands for $\mathbf{KG}$.

[20] "Tr" stands for the trace and $\mathbf{R} = \mathbb{I}_{N_t} - \mathbf{G}^\star\left(\mathbf{G}^{\star\prime}\mathbf{G}^\star\right)^{-1}\mathbf{G}^{\star\prime}$.

Because the denominator of T_{tf} does not follow exactly a Chi-squared distribution and is not totally independent from the numerator, we can not directly perform a statistical test on T_{tf} based on the Stutent's t-distribution. To address this issue, we use the Satterthwaite approximation which consists in approximating the denominator of (17) by a Chi-squared distribution and evaluate its degrees of freedom from the two first moments of $\tilde{\sigma}^2_{tf}$ i.e.

$$N_{tf} = \frac{\mathrm{Tr}(\mathbf{RKK}')^2}{\mathrm{Tr}(\mathbf{RKK}'\mathbf{RKK}')}. \tag{18}$$

In this approximation, T_{tf} is assumed to follow a Stutent's t-distribution with N_{tf} degrees of freedom and we can apply the statistical tests described in Sec. 3.1 on T_{tf} instead of T. As we will see below, the longer σ_t is the lower N_{tf} is. Therefore, the statistical test can become more conservative when we apply a time filtering on the data.

The result of the time filtering is illustrated in Figs. 18 and 19 which show a false color representation and the histogram of the local $T_{tf}(\mathbf{r})$ values computed after the full process (Fig. 11) with $\sigma_t = 0$ (no time filtering) and $\sigma_t = 1$ s for the artificial (Sec. 2.5) and the measured data (Sec. 2.4). As expected, thanks to the time filtering, the distribution of the T_{tf} values is renormalized. Nevertheless, it can deviate from the perfect Student's t-distribution since the denominator of (17) is not exactly a Chi-squared distribution. As a result, the number of type I errors decreases remarkably while the lost of sensitivity becomes critical. In particular, all the relevant detected excitations in the experimental data vanish (see Fig. 19). A finer tuning of the parameter σ_t could probably solve this issue. Nevertheless, in an ideal computation process all the parameters should be self-determined. It is why we present in the next section an other approach free of tunable parameters.

3.5.2 Time whitening

In opposite to the time filtering approach presented in the last section which imposes the time correlations to the data, the time whitening technique evaluates these correlations through an autoregressive model of order 1 [2, 24]. This model assumes that the error in the linear model (6) between two recorded images (i.e. $e(t_i)$ and $e(t_{i-1})$) are correlated such that

$$e(t_i) = \rho e(t_{i-1}) + u(t_i) \tag{19}$$

with $u(t_i)$ are independent random variables with $\mathrm{Var}(u(t_i)) = \sigma^2$. Within this model the components of the time correlation matrix $\mathbf{\Omega}$ are $\Omega_{ij} = \rho^{-|i-j|}/(1-\rho^2)$ and can be evaluated though the least square estimator of ρ:

$$\tilde{\rho} = \frac{\sum_i \tilde{e}(t_i)\tilde{e}(t_{i-1})}{\sum_i \tilde{e}(t_{i-1})^2} \quad \text{with} \quad \tilde{\mathbf{e}} = \tilde{\mathbf{I}} - \mathbf{G}\tilde{\boldsymbol{\beta}}. \tag{20}$$

Once ρ and $\mathbf{\Omega}$ are estimated, the general linear model (Sec. 3.1) is applied for the neuronal activation detection. Instead of computing[21] $\mathbf{\Omega}^{-1}$ and evaluate the T value according to Eqs. (7), (8) and (9), we apply the filter $\mathbf{\Omega}^{-1/2}$ with

$$\Omega^{-1/2}_{ij} = \begin{cases} 1 & \text{if } i = j \\ -\rho & \text{if } i - j = 1 \end{cases} \quad \text{and} \quad \mathbf{\Omega}^{-1/2\prime}\mathbf{\Omega}^{-1/2} = \mathbf{\Omega}^{-1} \tag{21}$$

on both $\tilde{\mathbf{I}}$ and $\mathbf{G}$ (i.e. $\tilde{\mathbf{I}} \rightarrow \mathbf{\Omega}^{-1/2}\tilde{\mathbf{I}}$ and $\mathbf{G} \rightarrow \mathbf{\Omega}^{-\mathbf{1/2}}\mathbf{G}$). This filtering decorrelates the data. The statistical test (9) using these corrected data and regressors is therefore performed by

[21] Considering boundary conditions $t_i = t_{i-N_t}$ if $i > N_t$, $\Omega^{-1}_{ij} = \begin{cases} 1 & \text{if } i = j \\ -\rho & \text{if } |i-j| = 1 \end{cases}$.

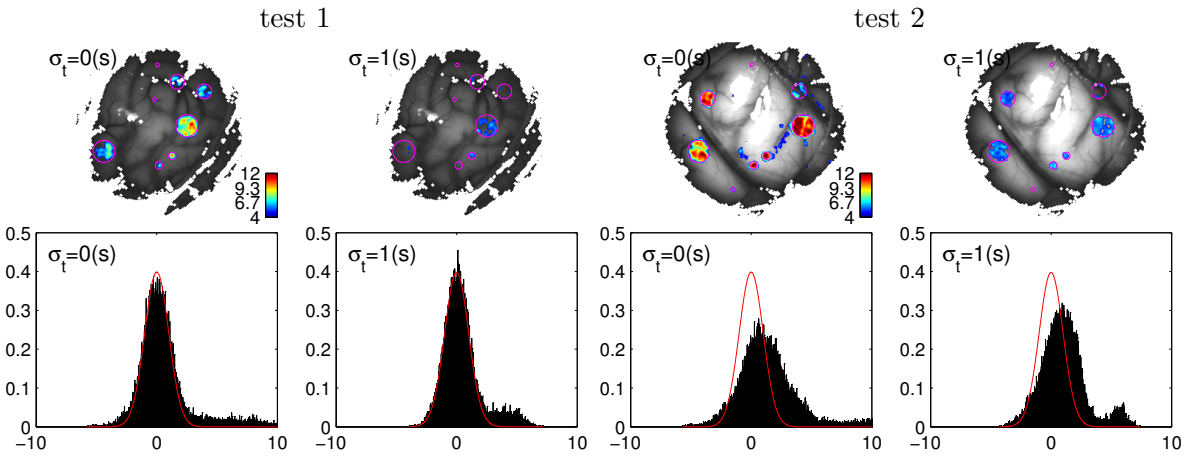

σ_t (s)	0	1
true excitations	1584	442
false excitations	103	21

σ_t (s)	0	1
true excitations	1932	1505
false excitations	1152	152

Figure 18: Test on two artificially computed data (test 1 and 2) (see Sec. 2.5). Each test includes: (figure above): False color representation of the local $T_{tf}(\mathbf{r})$ values (Eq. (9)) computed after the full detection process (see Fig. 7 with a time filtering) with $\sigma_t = 0$ (no time filtering) and $\sigma_t = 1$ s when the null hypothesis H_0 is rejected according to a one-tailed test (Eq. (10)) with $t_\alpha = 4.77, 5.13$ (for $\sigma_t = 0, 2$ s, $\alpha = 0.05$ and considering an optimal statistical criteria). The grayscale image represents the time average of the data and the white area is the omitted irrelevant area (Sec. 3.3). The pink circles locate the boundaries of the artificially added excitations. (figure below): Histogram of the T_{tf} values included in the relevant area. The red curve represents the expected Student's t-distribution with 374 and 73.3 degrees of freedom (for $\sigma_t = 0$ and 2 s). (table): Number of pixels rejecting the null hypothesis inside (true excitations) and outside (false excitations) the added excitations area. The false excitations are equivalent to the errors of type I and 2184 (number of artificially excited pixels) minus the true excitations correspond to the errors of type II.

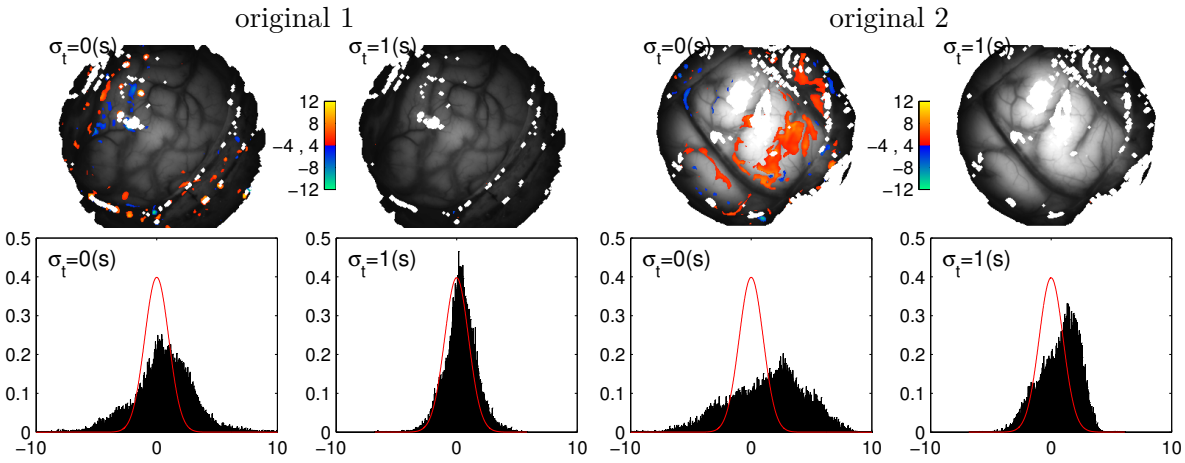

Figure 19: Same results as Fig. 18 but computed with the measured OIS (see Sec. 2.4) for $\sigma_t = 0$ (no time filtering) and $\sigma_t = 2$ s on two different patients (original 1 and 2) using a two-tailed test with $t_\alpha = 4.93, 5.33$ (for $\sigma_t = 0, 2$ s).

assuming that $\mathbf{\Omega} = \mathbb{I}_{N_t}$. As shown in Fig. 20, the Fourier transform of the filter $\mathbf{\Omega}^{-1/2}$ ($\hat{\Omega}^{-1/2}(\nu) = 1 - \rho e^{i2\pi\nu}$) is a bandpass filter which becomes stronger when the correlations are important ($\rho \lesssim 1$). As the frequency domain of the expected stimulation related OIS stands mainly in a low frequency band (see Fig. 4), the more correlated are the original data, the stronger decreases the whitened stimulation related OIS amplitude.

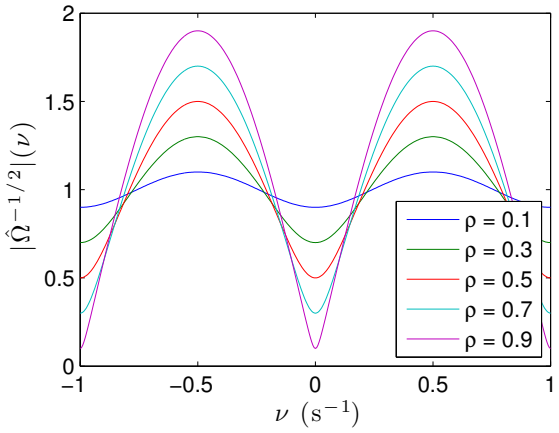

Figure 20: Spectral density of the time whitening filter $|\hat{\Omega}^{-1/2}|(\nu)$ for several values of ρ.

To investigate the spatial dependence of ρ, we evaluate $\tilde{\rho}$ independently on all the pixels (located in $\mathbf{r}$) of the recorded images. A grayscale representation of $\tilde{\rho}(\mathbf{r})$ (computed locally) is shown on Figs. 21 and 22 for the artificial (Sec. 2.5) and the measured data (Sec. 2.4), respectively. Although the artificial data underestimate the time and spatial correlations of the OIS[22], they show, in agreement with the measured data, that the correlations are stronger where the excitations are expected. This is principally due to the fact that the stimulation related OIS are not perfectly modelized by the first regressor in $\mathbf{G}$ which leads to an artificial increase in the time correlations and ρ where these stimulation related excitations are present. A local correction of the correlations by computing locally $\mathbf{\Omega}^{-1/2}$ would then decrease the sensitivity of the statistical test. It is why we estimate ρ globally i.e. by averaging the two terms of the ratio (20) on all the relevant pixels (Sec. 3.3) of the recorded images. By this way, the statistical fluctuations of ρ are minimized. Note also that ρ is locally increased by the spatial filtering when the spatial and time correlations of the measured OIS are both originally strong.

The effect of the time whitening is illustrated on Figs. 23 and 24 which show a false color representation and the histogram of the local $T(\mathbf{r})$ values computed after the full process (Fig. 11) with and without time filtering for the artificial (Sec. 2.5) and the measured data (Sec. 2.4), respectively. As discussed above, the artificial data being less correlated than the measured data, they show a smaller ρ which renormalizes the T value according to the expected Student's t-distribution. Thanks to the time whitening, the type I errors drastically decrease whereas the detection sensitivity is almost not modified by the time whitening. In opposite to the time filtering discussed in Sec. 3.5.1, the time whitening adapts the filter applied on the data according to the data correlations and is then more efficient. In the measured data, the time correlations are very strong, the resulting time whitening renormalizes then strongly the distribution of the measured T values which decreases the detection

[22]The origin of the correlations in the artificial data are both the motion, and the model of the excitations used in the detection process which is different from the artificially added excitations based on the linear response (Sec. 2.3).

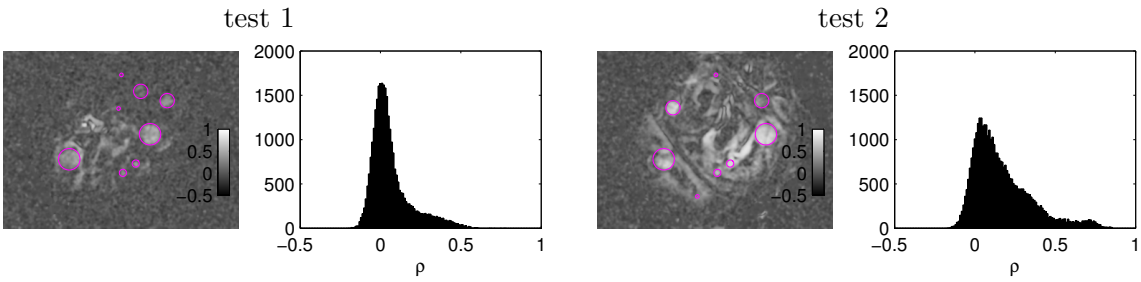

Figure 21: (left): Grayscale representation of the local estimation of $\rho(\mathbf{r})$ computed on the two artificial data sets (test 1 and 2) (see Sec. 2.5) after the spatial filtering (in the process shown in Fig. 7). The pink circles locate the artificially added excitations. (right): Histogram of the local $\rho(\mathbf{r})$ located in the relevant area (Sec. 3.3).

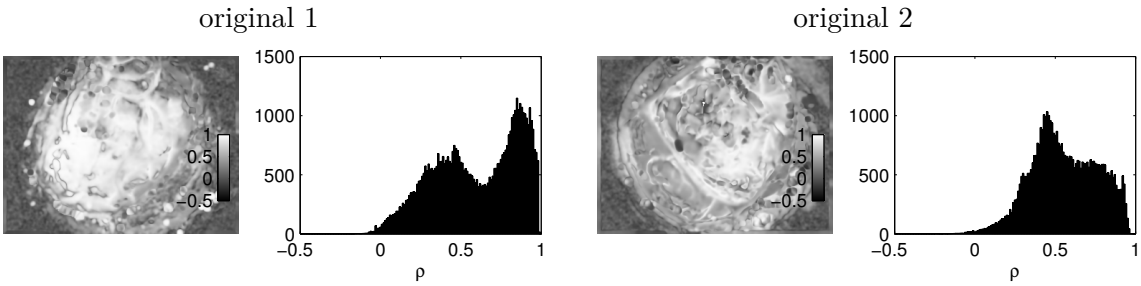

Figure 22: Same results as Fig. 21 but computed with the measured OIS (see Sec. 2.4) on two different patients (original 1 and 2).

sensitivity. Nevertheless, unlike the time filtering, small relevant detection area remains after the time whitening (see Fig. 24).

3.6 Wavelet

The spatial correlations of the data are problematic for a correct statistical detection of the excitations based on the assumption of independent variables. Although the spatial filtering discussed in Sec. 3.4 tends to uniform these correlations and adapts the statistical test according to that, this technique yields to an increase in the time correlations and then a decrease of the detection sensitivity. In addition, as the expanse of the neuronal excitation remains unknown, the choice of the filter size is arbitrary and not necessary adapted to all the stimulated cortical area.

An alternative way for dealing with these spatial correlations is to change the basis for representing the data and choose a multiscale representation which minimizes the number of correlated time series. As proposed in Ref. [19] for the analysis of fMRI data, the wavelet decomposition [11, 12] provides such a remarkable orthonormal basis. In this basis the local OIS temporal series are formulated as

$$\mathbf{I}(\mathbf{r}) = \sum_k \mathbf{I}_w(k)\ \psi_k(\mathbf{r}) \tag{22}$$

where $\psi_k(\mathbf{r})$ is the k^{nd} vector of the wavelet basis and $\mathbf{I}_w(k)$ is the related OIS temporal series. The multiscale structure of the basis ψ_k allows us to treat equitably the different sizes of the neuronal excitations such that the time series decomposed in this basis ($\mathbf{I}_w(k)$) are

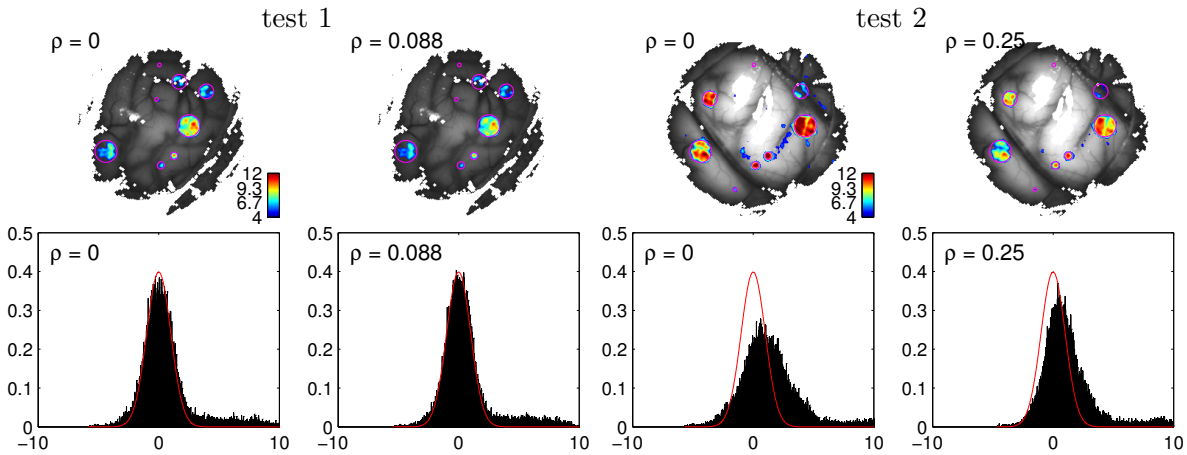

	no whitening	whitening
true excitations	1584	1457
false excitations	103	57

	no whitening	whitening
true excitations	1932	1758
false excitations	1152	439

Figure 23: Test on two artificially computed data (test 1 and 2) (see Sec. 2.5). Each test includes: (figure above): False color representation of the local $T(\mathbf{r})$ values (Eq. (9)) computed after the full detection process (see Fig. 7) with or without time whitening when the null hypothesis H_0 is rejected according to a one-tailed test (Eq. (10)) with $t_\alpha = 4.77$ ($\alpha = 0.05$ and considering an optimal statistical criteria). The grayscale image represents the time average of the data and the white area is the omitted irrelevant area (Sec. 3.3). The pink circles are the boundaries of the artificially added excitations. (figure below): Histogram of the T values included in the relevant area. The red curve represents the expected Student's t-distribution with 374 degrees of freedom. (table): Number of pixels rejecting the null hypothesis inside (true excitations) and outside (false excitations) the added excitations area. The false excitations are equivalent to the errors of type I and 2184 (number of artificially excited pixels) minus the true excitations correspond to the errors of type II.

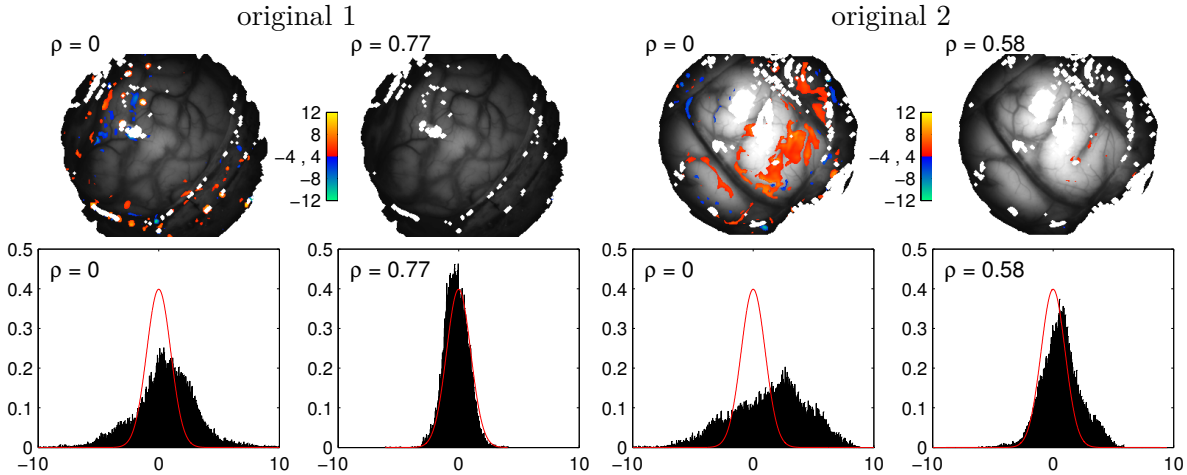

Figure 24: Same results as Fig. 23 but computed with the measured OIS (see Sec. 2.4) with and without time whitening on two different patients (original 1 and 2) using a two-tailed test with $t_\alpha = 4.93$.

decorrelated. As represented in Fig. 25, the wavelet decomposition has a pyramidal structure. The data are filtered spatially with complementary filters to separate the vertical, horizontal and uniform high frequencies from the low frequency components. This decomposition is then reiterate recursively on the low frequency components. Between each level of the wavelet decomposition, the spatial resolution of the data is divided by two. As illustrate in Fig. 26 on the time average of the OIS, this decomposition generates coefficients which represent the details of the data at different level of resolution. Therefore, a broad neuronal excitation is decomposed in a small number of wavelet coefficients $\mathbf{I}_w(k)$ as for a tight excitation both in the corresponding level of resolution. Thus in opposite to the spatial description, in which the time series are expressed in a local basis and have then correlations mainly related the size of the neuronal activity, only few wavelet coefficients $\mathbf{I}_w(k)$ are correlated with each others. The wavelet decomposition provides then quasi independent variables for performing the statistical test (Sec. 3.1).

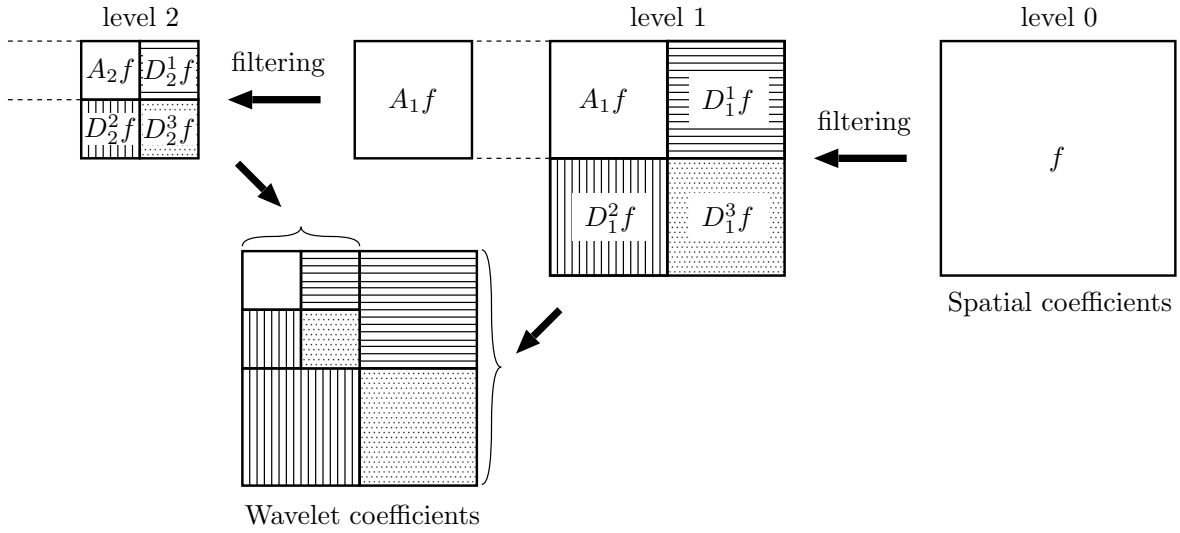

Figure 25: Pyramidal construction of the discrete wavelet transform. $D_j^1 f$, $D_j^2 f$, $D_j^3 f$ are the vertical, horizontal and uniform high frequency wavelet coefficients (spatial details) at the level j (with resolution 2^{-j}) of the function f. $A_j f$ are the low frequency wavelet coefficients (spatial average) at the level j of f.

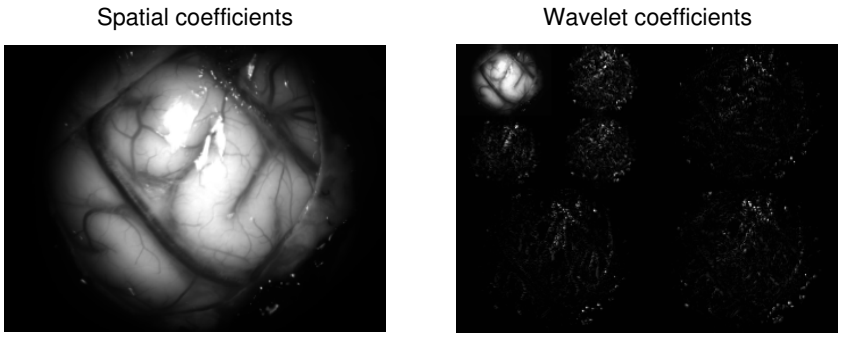

Figure 26: Time average of the OIS displayed in a spatial basis (left figure) and in a wavelet basis (right figure) down to 2 levels. The wavelet coefficients are represented as described in Fig. 25.

Nevertheless, in order to get an interpretation of the statistical test in the spatial basis, the detection process on the wavelet time series $\mathbf{I}_w(k)$ must be slightly modified from the "standard" process performed on the spatial coefficients and sketched in Fig. 7. Therefore, we follow Ref. [19] and split the statistical detection in two parts.

First, a denoising step based on the statistical significance of the wavelet coefficients is performed on the relevant first regressor $u_w(k) = \mathbf{c}'\boldsymbol{\beta}_w(k)$ where $\boldsymbol{\beta}_w(k)$ stands for the model parameters computed by (7) (or (15) after the time filtering) on the k^{nd} wavelet coefficients ($\mathbf{I}_w(k)$) of the OIS time series. Only the wavelet coefficients with $|T_w(k)| > \tau_w$ are kept with $T_w(k)$ stands for the T value computed by (9) (or (17) after the time filtering) on the k^{nd} wavelet components $\mathbf{I}_w(k)$ and τ_w is the wavelet threshold discussed below. Therefore, the denoised first regressor parameter in the spatial domain $u(\mathbf{r})$ becomes

$$u(\mathbf{r}) = \sum_k H(|T_w(k)| - \tau_w)\ u_w(k)\psi_k(\mathbf{r}). \tag{23}$$

with $H(x)$ is the Heaviside function.

Secondly, the statistical detection is performed in the spatial domain on the renormalized denoised first model parameter $u(\mathbf{r})/\Lambda(\mathbf{r})$ i.e.

$$\text{rejection when} \begin{cases} u(\mathbf{r})/\Lambda(\mathbf{r}) > \tau_s & \text{(one-tailed test)} \\ |u(\mathbf{r})|/\Lambda(\mathbf{r}) > \tau_s & \text{(two-tailed test)} \end{cases}. \tag{24}$$

The spatial renormalization factor $\Lambda(\mathbf{r}) = \sum_k \tilde{\sigma}_w(k)|\psi_k(\mathbf{r})|$ allows one to keep a spatial threshold τ_s constant although the sensitivity of the test changes after the wavelet denoising from pixel to pixel ($\tilde{\sigma}_w(k)$ stands for the error estimation computed by (8) (or (16) after the time filtering) on the k^{nd} wavelet time series $\mathbf{I}_w(k)$). The spatial and wavelet thresholds (τ_s and τ_w respectively) are determined by minimizing the difference between the denoised and the rough first regressor parameter while fixing the type I error (α/N_p considering the Bonferonni correction) in the spatial domain (see Ref. [19] for the technical details). Figure 27 shows the α dependence of these thresholds. Both τ_s and τ_w have a monotonic behavior with α. Although τ_w decreases with α (as t_α when a "standard" statistical test based on a Student's distribution is performed), t_s increases slightly with α.

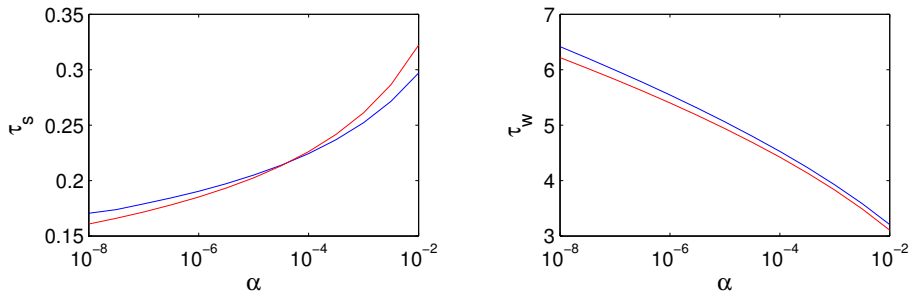

Figure 27: Spatial and wavelet thresholds (τ_s and τ_w respectively) versus α computed by considering that $T_w(k)$ follows a Student's t-distribution with $N = 374$ degrees of freedom (blue curves) and $N \to \infty$ equivalent to a normal distribution (red curves).

To compare the "wavelet" detection process with the "standard" method both sketched in Fig. 7, we show in Figs. 28 (artificial data) and 30 (measured data) a false color representation of $T(\mathbf{r})$ and $u(\mathbf{r})/\Lambda(\mathbf{r})$ and the histogram of the $T(\mathbf{r})$ and $T_w(k)$ values, respectively. In these examples, we perform the wavelet decomposition using the Daubechies wavelets of order 4

down to 3 levels and a time whitening step to decorrelate the wavelet time series. The results on the artificial data show that the wavelet process gives similar detection sensitivity than the "standard" method. Although the false detection errors are increased, this technique is free of tunable parameters (such as the size of the spatial filter σ_s in the "standard" method) and the time series are better decorrelated. As a result, the histogram of the T_w values fits better with the expected Student's t-distribution[23] and the autoregressive parameter ρ of the wavelet time series $\mathbf{I}_w(k)$ is much smaller (Figs. 29 and 31) compared to that computed with the spatial time series $\mathbf{I}(\mathbf{r})$ (Figs. 21 and 22). In addition, after the time whitening, the detected areas in the measured OIS which almost vanish in the full standard process (see Sec. 3.5.2) become more visible when the wavelet process is applied (see Fig. 30).

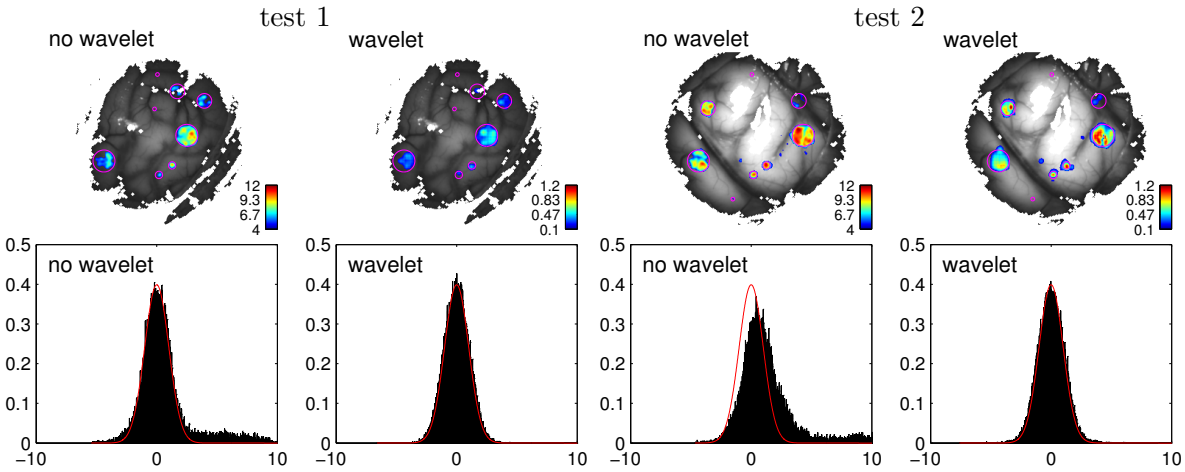

	no wavelet	wavelet
true excitations	1457	1367
false excitations	57	120

	no wavelet	wavelet
true excitations	1758	1830
false excitations	439	787

Figure 28: Test on two artificially computed data (test 1 and 2) (see Sec. 2.5). Each test includes: (figure above): False color representation of the local $T(\mathbf{r})$ (no wavelet) and $u(\mathbf{r})/\Lambda(\mathbf{r})$ values (wavelet) computed after the full "standard" and "wavelet" detection processes shown in Fig. 7 when the null hypothesis H_0 is rejected according to a one-tailed test. The grayscale image represents the time average of the data and the white area is the omitted irrelevant area (Sec. 3.3). The pink circles are the boundaries of the artificially added excitations. (figure below): Histogram of the $T(\mathbf{r})$ (in the relevant area) and $T_w(k)$ values, for the standard and wavelet process, respectively. The red curve represents the expected Student's t-distribution with 374 degrees of freedom. (table): Number of pixels rejecting the null hypothesis inside (true excitations) and outside (false excitations) the added excitations area. The false excitations are equivalent to the errors of type I and 2184 (number of artificially excited pixels) minus the true excitations correspond to the errors of type II.

Two improvements of this wavelet method are given in Ref. [20] i.e. the bias correction and the shift invariance of the inverse wavelet reconstruction. Nevertheless, as these do not give significant improvement of the detection sensitivity and the false detection minimization we do not show the results here.

[23]The bias in the estimation of ρ (Eq. 20) or the limit of validity of the autoregressive model to describe the noise in the temporal series can lead to an over renormalization of the T_w distribution (see Fig. 30).

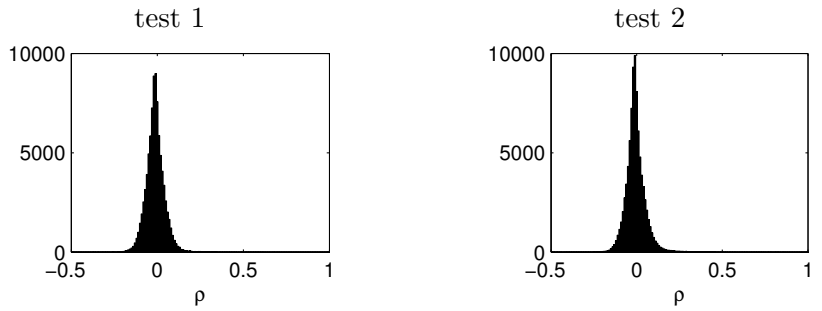

Figure 29: Histogram of the $\rho(k)$ computed on the wavelet time series $\mathbf{I}_w(k)$ of the two artificial data sets (test 1 and 2).

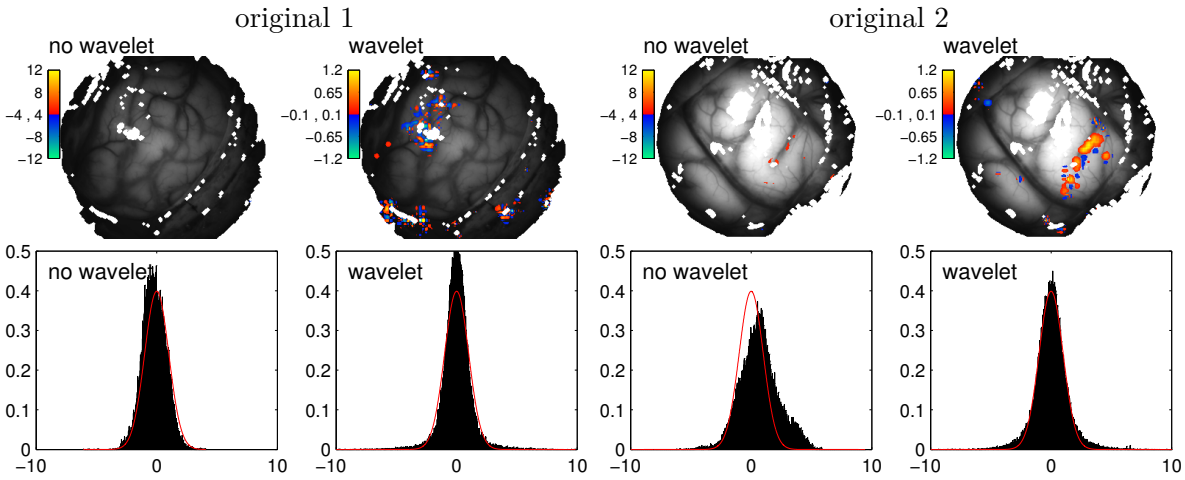

Figure 30: Same results as Fig. 28 but computed with the measured OIS (see Sec. 2.4) on two different patients (original 1 and 2) using a two-tailed test.

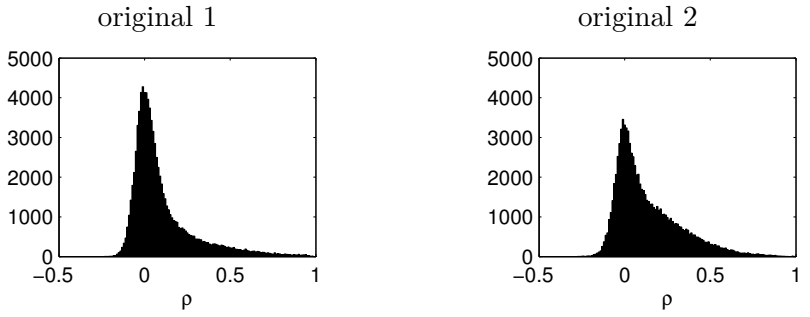

Figure 31: Histogram of the ρ computed on the wavelet time series $\mathbf{I}_w(k)$ of the two measured OIS (original 1 and 2).

4 Software description

Based on the methods described in Sec. 3, we implemented a user interface "OIS detection" in Matlab which allows to compute and visualize the detected area. The graphical interface is shown in Fig. 32 with the explanations of its visual components.

This tool allows to read the recorded images from the camera CCD written in a format `.sif` and the registrated time series saved in a format `.mha` after the time consuming

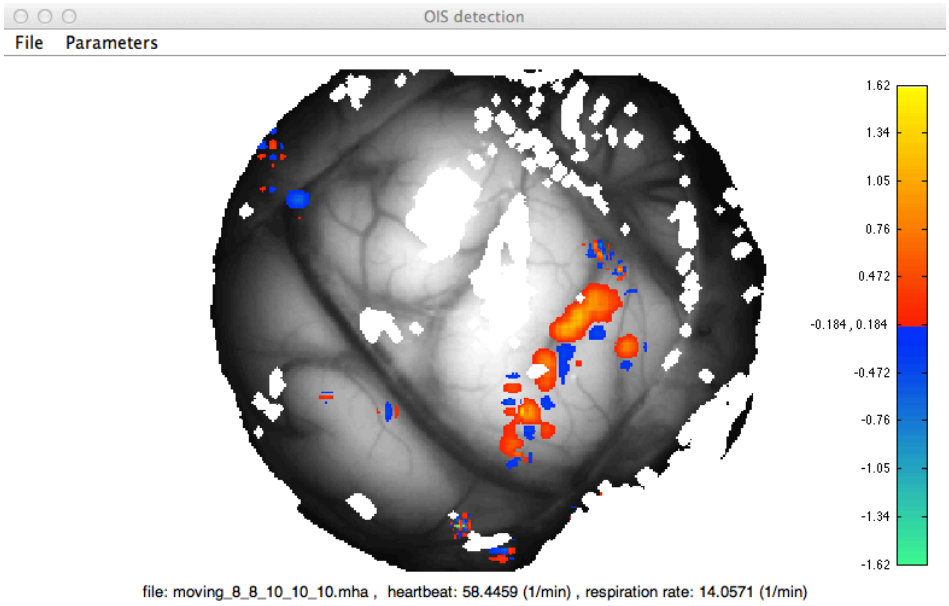

Figure 32: Main window of the OIS detection tool. The toolbar includes the "File" and "Parameters" menus for the file opening and the parameters setting, respectively. The file name of the processed data as well as the computed heartbeat and respiration rate are displayed on the bottom of the window. The white areas correspond to the irrelevant areas (see Sec. 3.3) and the colored pixels are the statistically relevant area. The color bar shows the color scale of the tested quantities $T(\mathbf{r})$ or $T_{tf}(\mathbf{r})$ (Eq. (9) or (17)) and $u(\mathbf{r})/\Lambda(\mathbf{r})$ (Eq. (23)) above the statistical threshold t_α and τ_s for the "standard" and "wavelet" detection process, respectively.

registration process performed on the raw data set.

The initialization parameters of the OIS detection tool for the data acquisition protocol and the computation process discussed in Secs. 2.4 and 3 are set in the files `acquisition_parameters.txt` and `detection_parameters.txt`, respectively. The most important parameters are also accessible directly in the programm through the "paramaters" menu in the toolbar and are summarized in the two next sections. Note that it is necessary to push the button "save" in the parameter setting windows in order to actualize the internal variables of the software before starting the detection process.

4.1 Acquisition parameters

For a correct use of the OIS detection tool, it is necessary to set precisely the parameters of the modelized OIS entering in the linear model (see Sec. 3.1). These parameters depend on the protocol and the type of the detected neuronal activity we focus on. They are summarized in the following list:

delta t acquisition: the elapsed time in (s) between the image acquisitions.

protocol: the acquisition protocol depends on the type of detected neuronal excitations:

- **stimulation:** the detection of the periodic stimulation related excitations discussed in Sec. 2.4 has to be set with the parameters:
  - **activation duration:** the duration of the stimulation in (s).

rest duration: the duration of the rest following the stimulation in (s).

number of blocks: the number of blocks (activation + rest) in the recorded data.

seizure: the detection of an epilepsy requires to record continuously a rest and a seizure period. Once parametrized, only the data included in these periods are kept for the analysis. If the rest period precedes the seizure, the following parameters are necessary:

rest start: the start of the rest period in (s) measured from the beginning of the data acquisition.

rest end: the end of the rest (or onset of the seizure) in (s) measured from the beginning of the data acquisition.

seizure end: the end of the seizure in (s) measured from the beginning of the data acquisition.

In opposite, if the seizure precedes the rest period:

seizure start: the onset of the seizure in (s) measured from the beginning of the data acquisition.

seizure end: the end of the seizure (or start of the rest period) in (s) measured from the beginning of the data acquisition.

rest end: the end of the rest period in (s) measured from the beginning of the data acquisition.

4.2 Detection parameters

The main parameters of the detection methods discussed in Sec. 3 and accessible in the user interface are summarized in the following list:

size reduction: the reduction of the data size by two in the two spatial directions (see Sec. 2.4).

registration: the registration of the raw images with the average of the time series (see Sec. 3.2). Once registrated, the data are saved.

wavelets: the choice of the detection process (with or without wavelet decomposition as discussed in Sec. 3). If the "wavelet" process is chosen the two improvements of the method discussed in Ref. [20] are possible:

invariance correction: this correction intends to recover the translation invariance of the detection process while the wavelet detection process discussed in Sec. 3.6 is not translational invariant.

bias correction: this correction intends to correct the artifacts of the wavelet reconstruction.

spatial filter: the spatial filtering requires the setting of the standard deviation σ_s in (pixel) of the gaussian filter (see Sec. 3.4).

time filter: the time filtering requires the setting of the standard deviation σ_t in (s) of the gaussian filter (see Sec. 3.5.1).

time whitening: the time whitening discussed in Sec. 3.5.2.

statistical test: the choice between a one- or two-tailed statistical test (see Sec. 3.1) for the activation detection.

significance level: the probability of assumed type I errors which set the threshold of the statistical test and the wavelet denoising (see Secs. 3.1 and 3.6).

5 Conclusions

In this report, we presented the statistical tool "OIS detection" that we have implemented for the analysis of OIS and the detection of neuronal excitations. By testing different algorithms we were able to optimize the detection sensitivity of stimulation related OIS and improve the computational time for applications in an intraoperative environment.

We showed that a registration step before performing the statistical detection was necessary for correcting the cortical movement. In addition, to make the calculation time reasonable during the surgery, we propose a parallelized version of this precomputational step. Furthermore, in order to deal with the correlations and to reduce the noise in the data we included in the detection process a wavelet decomposition and a time whitening steps. These techniques intend to decorrelate the data instead of imposing the correlations by a standard filtering and provide then a more sensitive detection. Moreover, these techniques do not need tunable parameters which make the detection process more robust. As a preliminary test for the validation of our detection tool, we checked that the detected area in the data "original 2" are in agreement with the direct electric cortical stimulation.

Although our detection process is already quite efficient, several improvements of the statistical tool remain possible. For example, in order to correctly detect the stimulation or the epilepsy related OIS a precise model of the expected signal is required. In this work, because the details of the measured OIS in humans is only poorly known, we simply used the electric stimulation or an Heaviside function as model. A better understanding of these signals in humans is then strongly required in order to improve our modelized OIS and then the quality of the detection.

To decorrelate in time the data, we assumed in the time whitening step that these correlations follow an autoregressive model of order 1. Although this model adapts the effect of the time whitening to the measured data, a more detailed model such as an higher order autoregressive model [6] or considering more complex correlation structures could improve the decorrelation step and therefore the detection process. In addition, for stability reasons and due to the chosen OIS model discussed above (see Sec. 3.5.2), the time correlations are considered globally in this work. It could be interesting to improve the detection tool by computing locally the parameters of the temporal correlation model such as in Ref. [24]. The estimation of the correlation parameters could also be improved by using an expectation maximization (EM) algorithm discussed in [8].

From an experimental point of view, for a better stability of the light environment and in order to minimize the glares in the recorded images, a circular light has been build to illuminate the cortical area with a larger incident angle during the measurements. A more diffuse illumination could be also set by adding a frosted glass below the light source. Furthermore, to minimize the cortical movement, it is planned to put piece of glass on the top of the cortex during the image recording. Nevertheless, for safety reasons the use of this glass should be avoided for the validation of the OIS technique on humans in an intraoperative environment.

References

[1] R. J. Adler and J. E. Taylor. *Random Fields and Geometry*. Springer, New-York, 2007.

[2] M. Bonneau and E. Leconte. Modèle linéaire. Polycopié de cours de statistique et économétrie, Université des sciences sociales, Toulouse.

[3] G. M. Boyntom, S. A. Engel, G. H. Glover, and D. J. Heeger. Linear systems analysis of functional magnetic resonance imaging in human v1. *The Journal of Neuroscience*, 16(13):4207–4221, 1996.

[4] C. H. Chen-Bee, T. Agoncillo, C. C. Lay, and R. D. Frostig. Intrinsic signal optical imaging of brain function using short stimulus delivery intervals. *Journal of Neuroscience Methods*, 187:171–182, 2010.

[5] K. J. Friston, J. T. Ashburner, S. J. Kiebel, T. E. Nichols, and W. D. Penny. *Statistical Parametric Mapping: The Analysis of Functional Brain Images*. Elsevier, London Burlington San Diego, 2006.

[6] K. J. Friston, O. Josephs, E. Zarahn, A. P. Holmes, S. Rouquette, and J.-B. Poline. To smooth or not to smooth? *NeuroImage*, 12:196–208, 2000.

[7] K. J. Friston, A. Mechelli, R. Turner, and C. J. Price. Nonlinear responses in fmri: The balloon model, volterra kernels, and other hemodynamics. *NeuroImage*, 12:466–477, 2000.

[8] K. J. Friston, W. Penny, C. Philips, S. Kiebel, G. Hunton, and J. Ashburner. Classical and bayesian inference in neurimagin: Theory. *NeuroImage*, 16:465–483, 2002.

[9] E. Hairer. Introduction à l'analyse numérique. Université de Genève.

[10] L. Ibánez, W. Schroeder, L. Ng, J. Cates, and *Insight Software Consortium*. The itk software guide. Second Edition, Updated for ITK version 2.4, 2005.

[11] S. Jaffard, Y. Meyer, and R. D. Ryan. *Wavelets Tools for Sciences and Technology*. SIAM, Philadelphia, 2001.

[12] S. G. Mallat. A theory for multiresolution signal decomposition: The wavelet representation. *IEE Transactions on pattern analysis and machine intelligence*, 11(7):674, 1989.

[13] *Open MP Architecture Review Board*. Openmp application program interface. Version 3.1, 2011.

[14] N. Pouratian, A. F. Cannestra, N. A. Martin, and A. W Toga. Intraoperative optical intrinsic signal imaging: a clinical tool for functional brain mapping. *Neurosurgical Focus*, 13(4):1, 2002.

[15] N. Pouratian, S. A. Sheth, N. A. Martin, and A. W. Toga. Shedding light on brain mapping: advances in human optical imaging. *TRENDS to Neurosciences*, 26(5):277, 2003.

[16] T. H. Schwartz, L. M. Chen, R. M. Friedman, D. D. Spencer, and A. W. Roe. Intraoperative optical imaging of human face cortical topography: a case study. *NeuroReport*, 15(9):1527, 2004.

[17] S. A. Sheth, M. Nemoto, M. Guiou, M. Walker, N. Pouratian, N. Hageman, and A. W. Toga. Columnar specificity of microvascular oxygenation and volume responses: Implications for functional brain mapping. *The Journal of Neuroscience*, 24(3):634–641, 2004.

[18] J.-P. Thirion. Image matching as a diffusion process: an analogy with maxwell's demons. *Medical Image Analysis*, 2(3):243–260, 1998.

[19] D. Van De Ville, T. Blu, and M. Unser. Integrated waveet processing and spatial statistical testing of fmri data. *NeuroImage*, 23:1472–1485, 2004.

[20] D. Van De Ville, M. L. Seghier, F. Lazeyras, T. Blu, and M. Unser. Wspm: Wavelet-based statistical parametric mapping. *NeurImage*, 37:1205–1217, 2007.

[21] K. J. Worsley. Local maxima and the expected euler characteristic of excursion sets of χ^2, f and t fields. *Adv. Appl. Prob.*, 26:13–42, 1994.

[22] K. J. Worsley, A. C. Evans, S. Marrett, and P. Neelin. A three-dimensional statistical analysis for cbf activation studies in human brain. In *Quantification of Brain Function: Tracer Kinetics and Image Analysis in Brain Pet*. Elsevier, 1993.

[23] K. J. Worsley and K. J. Friston. Analysis of fmri time-series revisited-again. *NeuroImage*, 2:173–181, 1995.

[24] K. J. Worsley, C. H. Liao, J. Aston, V. Petre, G. H. Duncan, F. Morales, and A. C. Evans. A general statistical analysis for fmri data. *NeuroImage*, 15:1–15, 2002.

[25] K. J. Worsley, S. Marrett, P. Neelin, A. C. Vandal, K. J. Friston, and A. C. Evans. A unified statistical approach for determining significant signals in images of cerebral activation. *Human Brain Mapping*, 4:68–73, 1996.